Title: Low thermal inertia of carbonaceous asteroid Bennu driven by cracks observed in returned samples

Authors: A. J. Ryan[1], R.-L. Ballouz[2], R. J. Macke[3], T. Ishizaki[4], A. Alasli[5], J. Biele[6], S. A. Eckley[7], C. G. Hoover[8], K. J. Jardine[8], A. J. King[9], C. P. Opeil[10], M. Pajola[11], F. Tusberti[11], J. J. Barnes[1], H. C. Bates[9], E. L. Berger[12], E. B. Bierhaus[13], C. Calva[7], S. Cambioni[14], F. Cheng[5], M. Delbo[15], D. N. DellaGiustina[1], J. P. Dworkin[16], C. M. Elder[17], J. P. Emery[18], J. Freemantle[19], R. Fujita[5], D. P. Glavin[16], C. Gonzalez[7], P. Haenecour[1], V. E. Hamilton[20], R. D. Hanna[21], L. T. J. Hanton[22], R. Harrington[7], A. R. Hildebrand[22], D. H. Hill[1], K. Ishimaru[1], E. R. Jawin[23], M. K. Kontogiannis[1], N. G. Lunning[12], T. J. McCoy[24], J. L. Molaro[25], M. Montoya[7], H. Nagano[5], E. W. O'Neal[7], J. Plummer[7], K. Righter[26], N. Sakatani[4], P. Sanchez[27], P. F. Schofield[9], M. A. Siegler[28], S. Tanaka[4], T. J. Zega[1], C. W. V. Wolner[1], H. C. Connolly[1,29,30] Jr. and D. S. Lauretta[1]

[1] Lunar and Planetary Laboratory, University of Arizona, Tucson, AZ, USA.
[2] Applied Physical Laboratory, Johns Hopkins University, Laurel, MD, USA.
[3] Vatican Observatory, Vatican City State.
[4] Japan Aerospace Exploration Agency (JAXA), Sagamihara, Japan.
[5] Department of Mechanical Systems Engineering, Nagoya University, Nagoya, Japan.
[6] German Aerospace Center, DLR-RB/MUSC, 51147 Cologne, Germany.
[7] Amentum-JETS2, Astromaterials Research and Exploration Sciences, NASA Johnson Space Center, Houston, TX, USA.
[8] School of Sustainable Engineering and the Built Environment, Arizona State University, Tempe, AZ, USA.
[9] Planetary Materials Group, Natural History Museum, London, UK.
[10] Department of Physics, Boston College, Chestnut Hill, MA, USA.
[11] INAF Astronomical Observatory of Padova, Padova, Italy.
[12] NASA Johnson Space Center, Houston, TX, USA.
[13] Lockheed Martin Space, Littleton, CO, USA.
[14] Department of Earth, Atmospheric, and Planetary Sciences, Massachusetts Institute of Technology, Cambridge, MA, USA.
[15] Université Côte d'Azur, CNRS, Observatoire de la Côte d'Azur, Laboratoire Lagrange, Nice, France.
[16] Solar System Exploration Division, NASA Goddard Space Flight Center, Greenbelt, MD, USA.
[17] Jet Propulsion Laboratory, California Institute of Technology, Pasadena, CA, USA.
[18] Department of Astronomy and Planetary Science, Northern Arizona University, Flagstaff, AZ, USA.
[19] Department of Earth & Space Science & Engineering, Lassonde School of Engineering, York University, Ontario, Canada.
[20] Southwest Research Institute, Boulder, CO, USA.
[21] Department of Earth and Planetary Sciences, Jackson School of Geosciences, The University of Texas at Austin, Austin, TX, USA.
[22] Department of Earth, Energy and the Environment, University of Calgary, Calgary, AB, Canada.
[23] Smithsonian Institution National Air and Space Museum, Washington, DC, USA.

[24] Department of Mineral Sciences, Smithsonian National Museum of Natural History, Washington, DC, USA.
[25] Planetary Science Institute, Tucson, AZ, USA.
[26] Department of Earth and Environmental Sciences, University of Rochester, Rochester, NY, USA.
[27] Colorado Center for Astrodynamics Research, University of Colorado Boulder, Boulder, CO, USA.
[28] Hawaiʻi Institute of Geophysics and Planetology, University of Hawaiʻi at Mānoa, Honolulu, HI, USA.
[29] Department of Geology, Rowan University, Glassboro, NJ, USA.
[30] Department of Earth and Planetary Sciences, American Museum of Natural History, New York, NY, USA.

Abstract

Thermal inertia is used to infer physical properties of asteroid surfaces. The carbonaceous asteroid Bennu has low thermal inertia suggestive of a surface covered in sub-centimeter rock fragments. However, spacecraft observations revealed that Bennu is instead blanketed by boulders of differing physical properties, with the most abundant population displaying very low thermal inertia compared to carbonaceous chondritic meteorites. Here we show that morphologically distinct particles in samples returned from Bennu also possess distinct thermal and physical properties, consistent with their genetic connection to the boulders. Angular particles have higher thermal inertia, greater hardness, and fewer but longer cracks that lead to more efficient splitting, relative to the hummocky particles. A hummocky particle exhibits low thermal inertia at sub-millimeter scales due to fine pores. Tortuous crack networks in hummocky particles further reduce thermal inertia while resisting disaggregation. Samples from Ryugu, a carbonaceous asteroid with similarly low thermal inertia, have cracks like those in Bennu's hummocky particles yet have bulk densities that indicate lower porosity. These observations imply that the low thermal inertia of both asteroids is driven by cracks in rocks resulting from geological processes within the parent body or, more recently, micrometeoroid impacts and thermal fatigue.

Main

Asteroids survive as remnants of the early Solar System, providing insight into the components and processes involved in the formation of primitive planetary bodies. They can also pose impact hazards to Earth, making it critical to understand their physical and mechanical properties to inform mitigation strategies (Michel, 2013 Bruck Syal et al., 2016; Cheng et al., 2018; Daly et al., 2023). Measurements taken at thermal infrared wavelengths offer insight into the physical properties of asteroid surfaces, often quantified in terms of the surface thermal inertia (Delbo et al., 2015). However, thermal inertia is controlled by many physical factors, complicating interpretation without complementary data (Emery et al., 2014; DellaGiustina & Emery et al., 2019). Planetary science missions have provided ground truth for remote observations with resolved images of asteroid surfaces and, more recently, returned samples (Nakamura et al., 2025).

NASA's OSIRIS-REx mission surveyed (101955) Bennu from 2018 to 2021 and delivered 121.6 g of its unconsolidated surface material ("regolith") to Earth on 24 September 2023 (Lauretta & DellaGiustina et al., 2019, 2022; Lauretta & Connolly et al., 2024). Bennu is a ~0.5-km-diameter rubble-pile asteroid composed of fragments from a larger (>100 km) parent body that was collisionally disrupted in the main belt (Walsh et al., 2013; 2024). Spacecraft observations of Bennu's boulder-covered surface (DellaGiustina & Emery et al., 2019) contradicted pre-arrival predictions of abundant sub-centimeter–scale particles (Lauretta et al., 2015) based on the relatively low thermal inertia of the body (310 ± 70 J m^{-1} K^{-1} $s^{-½}$) (Emery et al., 2014) and radar polarization ratio of its surface (Nolan et al., 2013).

Bennu's boulders can be broadly categorized into two populations (DellaGiustina et al., 2020; Rozitis et al., 2020). The most common boulders, especially in the largest size fraction (~10 m in diameter and larger), are very dark (normal reflectance of ~0.034–0.049) with rough or hummocky surfaces and sometimes clastic, layered textures (Ishimaru & Lauretta, 2024; Jawin et al., 2023). The comparatively bright boulder population—though still dark in an absolute sense (normal reflectance of ~0.049–0.074)—has smoother surfaces, sometimes pitted by impacts; higher angularity; and visible through-running fractures (DellaGiustina et al., 2020; Ballouz et al., 2020; Delbo et al., 2022; Jawin et al., 2023). Bright veins, interpreted as carbonate-bearing based on spectral data, occur within some boulders of the latter population, indicating localized fluid flow and complex aqueous alteration processes in Bennu's parent body (Kaplan et al., 2020).

Analysis of thermal infrared data collected by the spacecraft (Rozitis et al., 2020, 2022; Ryan et al., 2024) revealed that the dark boulders have exceptionally low thermal inertia (150–400 J m^{-1} K^{-1} $s^{-½}$) compared to meteorites and terrestrial rocks (~1000–3000 J m^{-1} K^{-1} $s^{-½}$) (Mellon et al., 2008; Opeil et al., 2012; Flynn et al., 2018). The brighter boulders have somewhat higher thermal inertia (400–1000 J m^{-1} K^{-1} $s^{-½}$), nearing those measured for ostensibly analogous carbonaceous chondrites (Rozitis et al., 2020, 2022; Opeil et al., 2020; Jawin et al., 2025). The dark boulders were inferred to have higher porosity, with the pores reducing bulk density, thermal conductivity, and thus thermal inertia, in comparison to the brighter ones (Rozitis et al., 2020). Further, the dark boulders were proposed to be less rapidly comminuted by space weathering processes such as impacts and thermal fatigue, compared to the denser but more readily cleavable bright boulders (Cambioni et al., 2021). The samples returned to Earth likely comprise fragments of both boulder populations, based on visual (Jawin et al., 2023; Lauretta et al., 2022) and thermal (Ryan et al., 2024) analysis of the sample site.

Particles in the Bennu sample collection can be categorized into at least three major types based on morphology, apparent brightness, and petrology (Lauretta & Connolly et al., 2024; Connolly & Lauretta et al., 2025), with similarities to Bennu's boulders despite the difference in scale: (i) "Hummocky" particles are rough and nodular, resembling the dark boulders with the lowest thermal inertia. (ii) "Angular" particles are smoother, with distinctive flat faces, resembling the brighter boulders with higher thermal inertia. (iii) The rarer "mottled" particles are characterized by bright mineral coatings and veins; they may be a subtype of the angular particles, sampling vein-rich regions of the brighter boulders (Lauretta and Connolly et al., 2024; Connolly & Lauretta et al., 2025). Initial measurements indicated distinct densities among the three types, in increasing order from hummocky, to angular, to mottled (Lauretta & Connolly et al., 2024), suggestive of distinct thermal properties.

The Bennu samples share mineralogical similarities with those from carbonaceous asteroid (162173) Ryugu and the Ivuna-type (CI) carbonaceous chondrites (Lauretta & Connolly et al., 2024; Connolly & Lauretta et al., 2025; Zega & McCoy et al., 2025), all of which are characterized by having experienced extensive aqueous alteration. In addition, the dark boulders on Bennu and Ryugu have similar morphology and thermal properties, suggesting that the boulders' internal structures may also be similar (Grott et al., 2019; Okada et al., 2020; Rozitis et al., 2020). Laboratory measurements of Ryugu samples have yielded thermal inertia values that are higher by a factor of about 3.5 times than those inferred from remote sensing data collected by the Hayabusa2 spacecraft. This finding suggests that the remotely sensed boulders have crack networks that either are larger than the length scale of the laboratory thermal measurements (several hundred microns) or were destroyed during sampling (Nakamura et al., 2023; Ishizaki et al., 2023; Hamm et al., 2025).

Here, we investigate the origin and implications of Bennu's low but varying thermal inertia by characterizing the physical and thermal properties of individual particles (1.5–5 mm in length) and aggregate material (bulk, unsorted mixtures of particles <5 mm in length) returned by OSIRIS-REx. We focus our analysis on the hummocky and angular particles because they may be genetically linked to the most common boulder types on Bennu; further, they are petrographically and petrologically distinct lithologies (Connolly & Lauretta et al., 2025), suggesting that they may also differ in their physical and thermal properties. This work investigates length scales that approach the remote sensing thermal wave penetration depth on Bennu (a few centimeters), providing the necessary context to better interpret telescopic and spacecraft observations.

Thermal and physical properties

We measured thermal diffusivity in vacuum in targeted locations on one hummocky particle (OREX-800118-0, 49 mg) and three angular particles (OREX-800055-7, OREX-800055-8, and OREX-803009-102, ~2–3 mg each) by lock-in thermography (LIT; Methods) (Figs. 1 and 2, Extended Data Table 1). This technique, which has also been used for analysis of Ryugu samples, involves no sample preparation, contamination, or destruction (Nakamura, 2023; Ishizaki et al., 2023) and is inherently sensitive to the effects of fine porosity. To convert thermal diffusivity into thermal conductivity and thermal inertia, we also needed to determine the specific heat — which depends on mineralogy and temperature — and the bulk density of the materials. We measured a representative specific heat using powder subsamples of a large, homogenized aggregate (OREX-800107-0, 6.425 g) via differential scanning calorimetry and the hybrid adiabatic relaxation heat capacity method (Methods, Extended Data Fig. 1). The bulk densities of several larger particles (0.049–2.9 g) were determined from volume measurements via structured light scanning (SLS) and X-ray computed tomography (XCT) (Methods, Extended Data Fig. 2, Extended Data Table 2), combined with their masses. The XCT data also provided insight into the internal structure of each sample, specifically internal void spaces (porosity). For clarity, herein we use "pores" to mean equant or irregular voids, distinct from cracks (sheet-like voids); both contribute to overall porosity.

The derived thermal inertia values of the hummocky particle are heterogeneous and have a lower mean and much lower minimum than those of the angular particles (minimum, mean, maximum: 260, 637, 970 J m^{-2} K^{-1} $s^{-½}$ and 710, 888, 1120 m^{-2} K^{-1} $s^{-½}$, respectively) (Figs. 1 and 2, Extended Data Table 1). XCT data from the hummocky particle reveal high concentrations of visible pores and cracks ~10–30 µm in size at the locations with the lowest thermal inertia (Fig. 3). In contrast, locations with higher thermal inertia generally show fewer or no visible pores or associated cracks. The angular particles do not display any areas of visible pores within the analysis regions (Fig. 3).

The hummocky and angular samples we analyzed have mean densities that are distinct at more than the 1-σ level — 1.54 ± 0.10 g cm^{-3} vs. 1.72 ± 0.07 g cm^{-3} (Extended Data Fig. 2, Extended Data Table 2) — consistent with previous analyses (Lauretta & Connolly et al., 2024). This suggests that they may have systematic differences in porosity and/or mineralogy, which could contribute to the difference in measured thermal diffusivity and derived thermal inertia. These values, coupled with Bennu's bulk density of 1.190 ± 0.018 g cm^{-3} (Scheeres et al., 2019), indicate that the bulk macroporosity of the asteroid is in the range of 23–31%. This is slightly lower than previous estimates of 25–50% (Scheeres et al., 2019; Barnouin et al., 2019; Lauretta & DellaGiustina et al., 2019) based on data from CI and Mighei-type (CM) meteorites, both of which have higher bulk densities than Bennu's hummocky material (Extended Data Fig. 2). However, it is still consistent with Bennu being a rubble-pile asteroid (Grott et al., 2020) yet with fewer large voids than previously expected (Scheeres et al., 2020). Rather, a large fraction of the asteroid's total porosity is contained in boulder microporosity.

To estimate microporosity and total porosity, we calculated an average sample grain density of 2.8 ± 0.1 g cm^{-3} from X-ray diffraction (XRD)–derived mineralogy of subsamples from two large, homogenized aggregates (OREX-800107-0, 6.425 g, and OREX-800117-0, 1.288 g; Methods, Extended Data Table 3). The microporosity of angular and hummocky particles could thus range from approximately 39 to 45%, though it is not yet known how potentially systematic variations in mineralogy between them could impact those values. Nonetheless, we use the average sample grain density to estimate a total porosity of ~58% for Bennu, within range of predictions from spacecraft observations (50–60%; Barnouin et al., 2019).

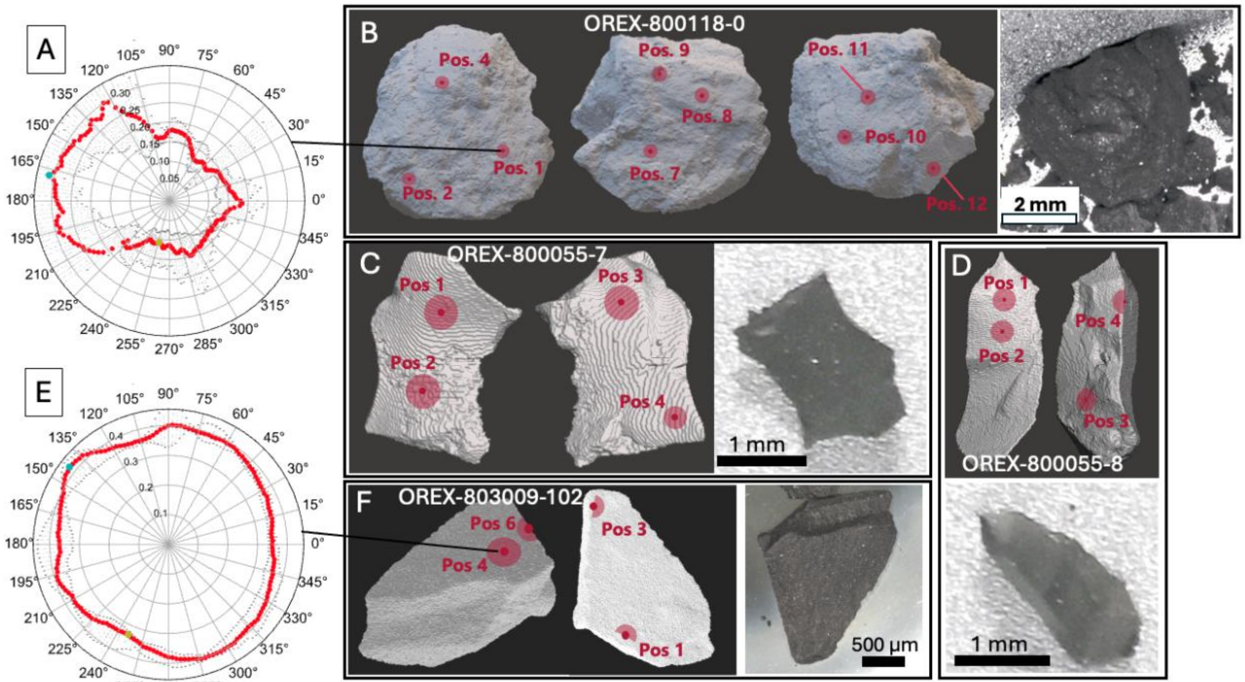

Figure 1. Lock-in thermography (LIT) measurements of thermal diffusivity in hummocky and angular samples. **(A)** LIT thermal diffusivity distribution for Position 1 on hummocky sample OREX-800118-0. The radial coordinates of the polar plot indicate the thermal diffusivity values (units of square millimeters per second), which are obtained surrounding the laser heating spot on the sample as a function of the circumferential azimuth angle. **(B)** LIT measurement positions overlain on an XCT shape model of OREX-800118-0, accompanied by an optical image of the particle. **(C)** As in (B), but for angular sample OREX-800055-7. **(D)** As in (B), but for angular sample OREX-800055-8. **(E)** LIT thermal diffusivity distribution for Position 4 on angular sample OREX-803009-102. **(F)** As in (B), but for angular sample OREX-803009-102.

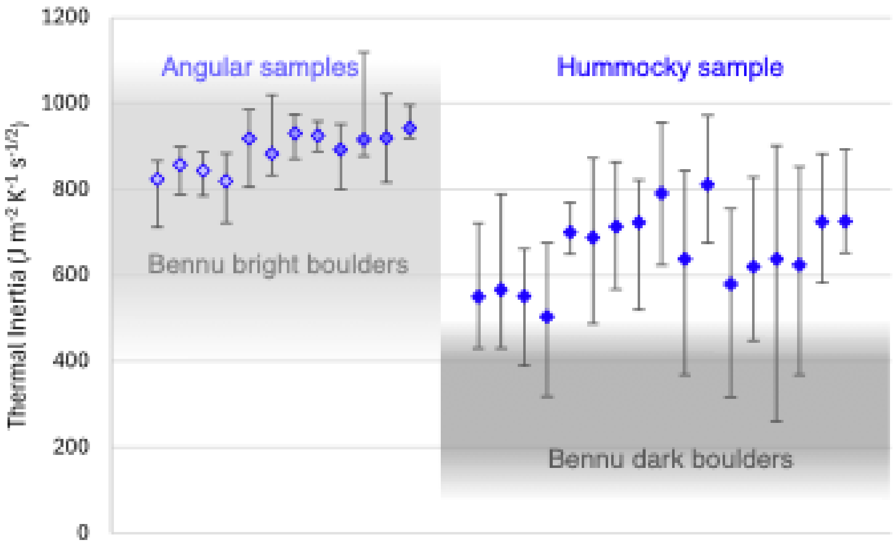

Figure 2. Thermal inertia of Bennu particles obtained by LIT, compared to that of Bennu boulders derived from remote sensing data. Three angular samples (left) were measured at

four distinct positions each, as shown in Fig. 1C, 1D, and 1F. One hummocky sample (right) was analyzed at nine positions (Fig. 1b), some with varying laser pulse frequencies to vary the length scale of measurement sensitivity. Values are reported in the order of position number, as shown in Fig. 1 and Extended Data Table 1. Error bars are based on the maximum and minimum diffusivity values measured at each analysis position. Gray shaded areas correspond to the thermal inertia ranges of the two main boulder populations derived from spacecraft data (Rozitis et al., 2020, 2022; Ryan et al., 2024; Jawin et al., 2025).

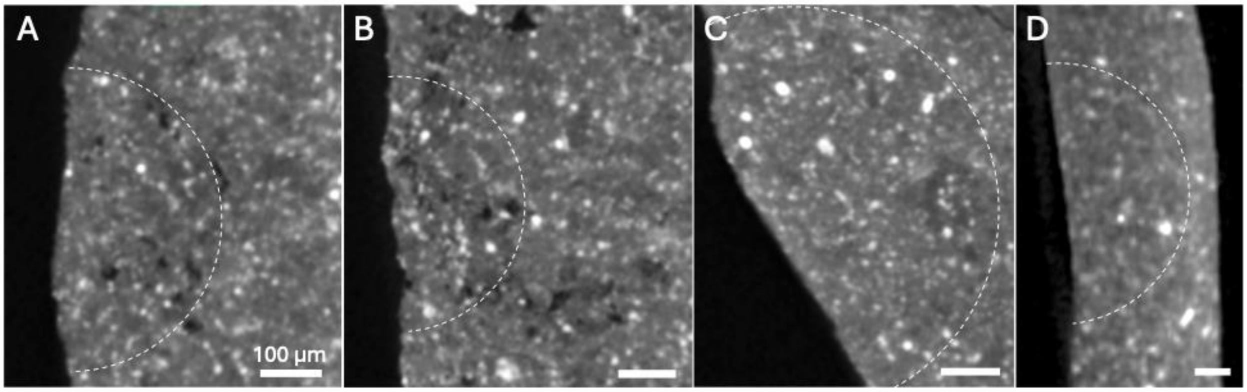

Figure 3. XCT scan slices of LIT analysis sites in hummocky and angular samples provide context for interpreting thermal diffusivity and thermal inertia results. All scale bars are 100 µm. The dashed lines represent an estimate of the thermal wave penetration extent (measurement sensitivity). All measurements shown were conducted with a 4 Hz laser pulse frequency, which translates to thermal waves of 220–360 µm. **(A, B)** Positions 1 and 2 in hummocky particle OREX-800118-0, which have low thermal diffusivity, low thermal inertia, and visible pores (dark voids). **(C)** Position 8 in hummocky particle OREX-800118-0, which has high thermal diffusivity, high thermal inertia, and no visible pores. **(D)** Position 4 in angular particle OREX-800055-7, which has high thermal diffusivity, high thermal inertia, and no visible pores.

Crack networks effects on thermal properties

Although the LIT measurements appear to have captured the effects on thermal properties of localized clusters of pores, it did not capture the effects of most cracks in the samples. More often than not, cracks were absent from the small volume of the sample probed by LIT at each measurement position. The LIT thermal wave was limited to ~100–850 µm based on the size of requisite naturally occurring flat surfaces and the thermal diffusivity of the material. In instances where cracks were present within the measurement volume, they were typically thermally resistive enough to completely impede the thermal wave. This had the effect of shortening the distance of measurement sensitivity, thereby excluding the thermal effects of the crack from the result, or even invalidating the result completely in instances where the crack reflected the thermal wave.

An extensive XCT dataset of several large particles (~0.05–2.25 g and ~0.5–2.0 cm), acquired at NASA's Johnson Space Center (JSC) (Methods), enables a more thorough examination of the interior structure of Bennu samples. The three-dimensional (3D) internal fracture networks within large hummocky and angular particles are typically distinct from each other (Fig. 4), which could cause their thermal properties at larger scales to further diverge from those measured at smaller scales by LIT. The angular particles generally feature fewer, longer, and straighter cracks, whereas hummocky particles are more densely populated with shorter, jagged, and disjointed cracks that often contour around or completely encapsulate distinct clasts. Concentrations of small pores, like those associated with lower thermal inertia in OREX-800118-0 (Fig. 3), are rarely visible in XCT data of angular particles, and in some hummocky particles are visible only in localized clusters.

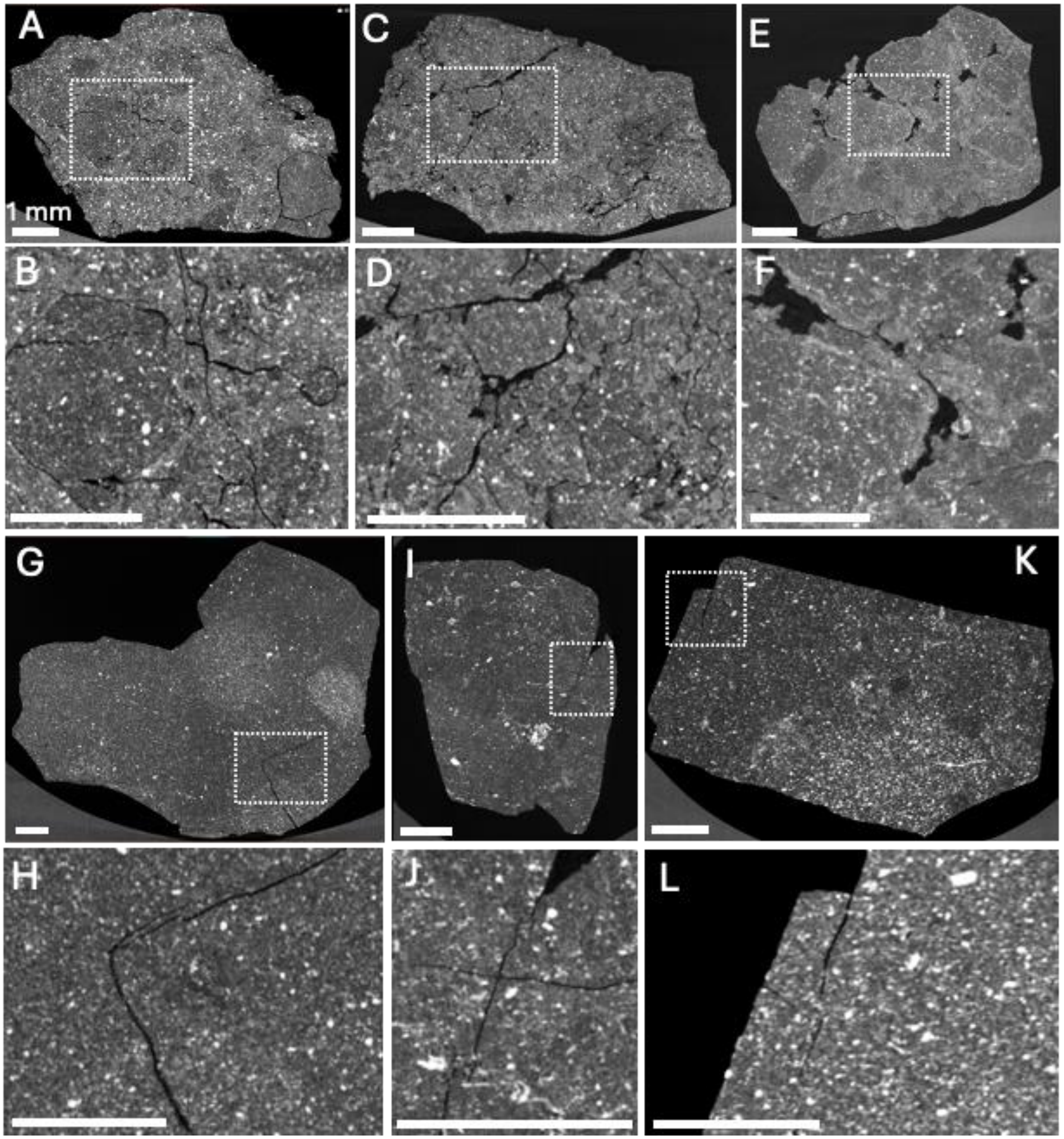

Figure 4. XCT scan slices of hummocky (A–F) and angular (G–L) particles, including zoomed-in images of characteristic cracks and voids. All scale bars are 1 mm. Dashed rectangles correspond to the closeup views in the panels below. **(A, B)** OREX-800088-0. **(C, D)**

OREX-800097-0. **(E, F)** OREX-800089-0. **(G, H)** OREX-800055-0. **(I, J)** OREX-800054-0. **(K, L)** OREX-800047-0.

To assess the importance of cracks on thermal inertia, we simulated heat flow using crack networks directly extracted from XCT datasets of several large (168–592 mg) angular and hummocky particles (Methods) (Fig. 5). Our simulations indicate that the resolved crack networks in the hummocky particle can reduce thermal conductivity by as much as ~40% (a 23% reduction in thermal inertia), whereas the crack networks of angular particles reduce conductivity by at most ~10% (Extended Data Table 4). Many cracks, however, cannot be completely extracted from the XCT data due to resolution limits, resulting in artificial gaps within the crack networks through which heat could flow in our simulations.

Given the potential importance of the crack networks in influencing sample thermal properties, we considered whether the cracks were pre-existing or formed during sample collection and return. Seven angular and mottled particles (all larger than ~1 cm) within the sample collection were found to fit together like puzzle pieces based on feature matching in images and/or 3D scan data reconstruction (Methods, Extended Data Fig. 3), indicating that some breaking likely occurred during sampling and/or Earth return. However, the power-law index of the sample particle size frequency distribution (PSFD; Methods), –2.1 ± 0.3 for particles larger than 1.1 mm, closely resembles that of the OSIRIS-REx sample site (–2.2 ± 0.01 between approximately 50 and 300 mm) (Burke et al., 2021) (Fig. 6, Extended Data Fig. 4). Thus, despite the observation of puzzle-piece particles, most of the sampled material probably was not extensively modified during acquisition and/or delivery to Earth; otherwise, a steepening of the power-law index in the finer size fractions should be observed.

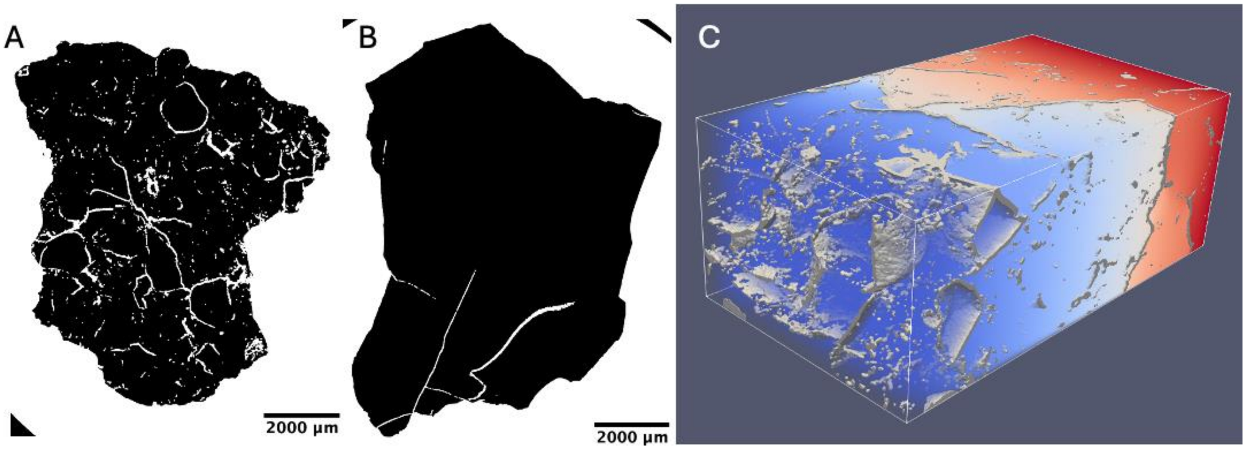

Figure 5. Extraction of cracks from XCT scans of hummocky and angular particles and thermal modeling to assess their impact on thermal inertia. Representative crack network masks from XCT segmentation from **(A)** a hummocky particle (OREX-800088-0) and **(B)** an angular particle (OREX-8000055-0). (**C**) Steady-state modeled temperature field through a rectangular region cropped from the center of OREX-800088-0, with cracks and voids rendered in gray. The color represents temperature in arbitrary units. Abrupt drops in temperature are due to the high thermal resistivity and lateral continuity of the cracks. The longest axis of the box is 6.2 mm.

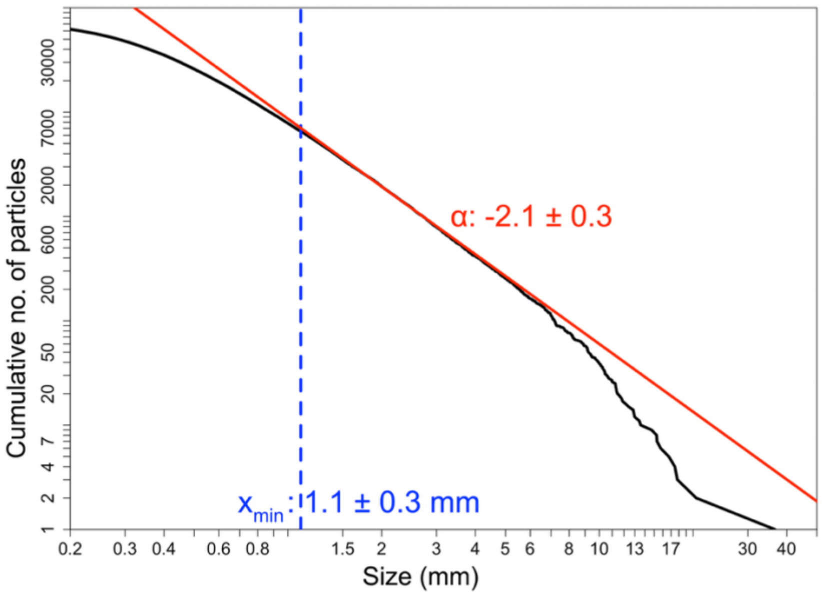

Figure 6. Particle size frequency distribution of the Bennu sample. The cumulative PSFD (black line) results from the manual measurement of the longest axis of 72,776 particles ranging from 0.03 to 36.6 mm. The distribution is fit by a power-law function (straight red line, exponent $\alpha = -2.1 \pm 0.3$) with a completion limit of $x_{\min} = 1.1 \pm 0.3$ mm.

Mechanical properties

The differences in crack networks and bulk density between angular and hummocky particles suggest that they may have distinct structural and mechanical properties. To investigate this, representative particles from the two lithologies were split with a chisel (Methods, Extended Data Fig. 5) in the OSIRIS-REx cleanroom at JSC. The angular particle (OREX-800055-0; 591 mg) primarily split along long, smooth, or planar pre-existing fractures, producing fragments resembling the parent particle, and in some cases exhibiting platy or bladed morphologies. Nearly all pre-existing cracks resulted in breaks, indicating a high susceptibility to comminution in response to an external stimulus. The hummocky particle (OREX-800088-0; 329 mg) also split mostly along pre-existing fractures, creating similarly hummocky fragments, but many pre-existing cracks were left unutilized. Despite having far more numerous and tightly spaced cracks than its angular counterpart, the hummocky particle did not produce a greater number of fragments when split. This implies a geometric interlocking of materials, even when already densely cracked. Further, these controlled splits indicate that the external morphology of the two lithologies directly reflects their differing internal crack styles, as the morphology of the generated particles was dictated by the nature of pre-existing internal cracks. The morphological similarity between samples and boulders (Lauretta & Connolly et al., 2024) despite a difference of many orders of magnitude in scale suggests that crack morphology may also be scale-independent. Finally, we did not observe any new cracks within the interiors of fragments from the controlled splits, indicating that cracking generally leads to failure in this context.

We performed nanoindentation measurements (Methods) of the fine-grained matrix in fragments derived from the controlled splits. OREX-800055-9, an angular fragment, yielded an elastic modulus (*M*) and indentation hardness (*H*) of 15.86 ± 3.41 GPa and 0.400 ± 0.123 GPa, respectively. OREX-800088-5, a hummocky fragment, yielded *M* and *H* of 11.82 ± 2.35 GPa and 0.244 ± 0.065 GPa, respectively. These results indicate that the matrix in the hummocky fragment was more compliant, lower in strength, and more ductile than the angular fragment.

Discussion

The analysis of returned samples from Bennu and Ryugu permits a ground-truthing of findings from remote sensing data. In particular, the physical mechanism responsible for the low thermal inertia of the dark boulders on both bodies has remained an unresolved question. Given that both asteroids' surfaces are dominated by boulders, rather than unconsolidated regolith, and that the boulders and samples of both asteroids share many similarities in appearance and composition (DellaGiustina & Emery et al., 2019; Shimaki et al., 2020; Rozitis et al., 2020; Yokoyama & Nagashima et al., 2023; Lauretta & Connolly et al. 2024; Connolly & Lauretta et al., 2025), it is plausible that their similarly low thermal inertia has a common explanation.

LIT measurements of Ryugu samples yielded higher mean thermal inertia values (791–1253 J m^{-2} K^{-1} $s^{-½}$) than those values obtained via remote sensing from orbit (225 ± 45 J m^{-2} K^{-1} $s^{-½}$) and from the surface (295 ± 13 J m^{-2} K^{-1} $s^{-½}$) (Shimaki et al., 2020; Hamm et al., 2020; Nakamura et al., 2023; Ishizaki et al., 2023). Although we found that angular Bennu samples have similarly high thermal inertia (710–1120 J m^{-2} K^{-1} $s^{-½}$), this is readily explained by their proposed linkage (Lauretta & Connolly et al. 2024) to Bennu's brighter, higher-thermal-inertia boulders (~400–1000 J m^{-2} K^{-1} $s^{-½}$) and does not necessarily connect Ryugu particles to the Bennu angular lithology.

The Bennu hummocky sample we studied exhibits a wider and somewhat lower range of thermal inertia values (260–970 J m^{-2} K^{-1} $s^{-½}$) than the Ryugu samples and the Bennu angular particles, with thermal inertias at some measurement positions consistent with Bennu's dark, low-thermal-inertia boulders (150–400 J m^{-2} K^{-1} $s^{-½}$). However, those lowest-thermal-inertia measurement sites, caused by clusters of pores (tens of micrometers in size), are less common than higher-thermal-inertia sites in that same sample. The pores, visible in XCT data, are not pervasive throughout the particle, which likely gives it a bulk thermal inertia near the higher end of the localized measurements. Furthermore, clusters of visible pores are not widespread in XCT data of other large hummocky particles. We considered whether higher-porosity particles were preferentially comminuted to smaller size fractions because of their potentially lower strength. However, we examined numerous small (<~5 mm) particles in XCT scans of aggregate samples (OREX-800107-0 and OREX-800117-0) and did not observe a higher abundance of clearly porous fabrics, suggesting that pore-induced low thermal inertia is a localized phenomenon.

In addition, Ryugu samples have generally higher bulk density values than Bennu's hummocky particles (Nakamura et al., 2023; Miyazaki et al., 2023) (Extended Data Fig. 2), suggesting that their overall porosity is lower. Therefore, although Bennu samples indeed exhibit localized instances of high matrix porosity which can lead to low thermal inertia values, the apparent scarcity of highly porous fabrics in these samples, coupled with the lower overall porosity of the Ryugu samples, suggests that matrix porosity alone may not fully account for the low thermal inertias of the two asteroids.

Our analysis identified cracks as a mechanism for lowering the thermal inertia of the samples, where Bennu's hummocky samples are more densely fractured and thus likely have thermal inertias further below what would be measured by LIT. The largest analyzed Ryugu particle (C0002) closely resembles hummocky Bennu particles; it contains abundant cracks (Extended Data Fig. 6) and has heterogeneous thermal inertia, similar to OREX-800118-0. The

LIT technique used to analyze C0002 (Ishizaki et al., 2023) is generally insensitive to the broader crack networks, because cracks are often too far from the measurement region or are so thermally resistive that they disrupt the dataset (Methods). However, a limited number of measurements in C0002 did capture the likely influence of proximal cracks, yielding low thermal inertia values (<300 J m^{-2} K^{-1} s$^{-½}$) (Ishizaki et al., 2023). These rare cases highlight the strong effect of nearby cracks, while reinforcing that the full influence of pervasive crack networks must be inferred through modeling rather than directly resolved by LIT.

Crack networks are therefore the most plausible requirement for producing the low thermal inertia observed on both bodies. In addition to the cracks, the fine-scale porosity (mostly unresolved in XCT) of the phyllosilicate-rich matrix sets the background thermal conductivity of the material, lowering thermal inertia from values typical of dense, less porous lithologies (~2000–2500 J m^{-2} K^{-1} s$^{-½}$, as in basalts or stony meteorites (Opeil et al., 2012; Mellon et al., 2008)) down to the range of ~700–1500 J m^{-2} K^{-1} s$^{-½}$ observed in Bennu angular particles, most Ryugu samples (Ishizaki et al., 2023), and aqueously altered carbonaceous chondrites (Opeil et al., 2020). The most aqueously altered carbonaceous chondrites have comparable densities (Macke et al., 2011) and conductivities (Opeil et al., 2020) to the Bennu and Ryugu samples, indicating that a high-porosity phyllosilicate matrix is a universal driver of low thermal inertia in aqueously altered astromaterials.

The relationship between porosity and thermal conductivity is highly complex and depends on the nature and distribution of pores, rather than their bulk volume alone. The pore and crack networks that we extracted from XCT data for our numerical thermal analysis can be used to obtain a rough estimate of visible pore and crack volume, which we find accounts for no more than 15% (often <2%) of the total internal porosity inferred from our bulk density and grain density measurements. This means that most porosity is unresolved at the XCT scale (approximately 6–10 µm/voxel in our datasets) but is likely captured in the LIT measurements, leading to lower derived thermal inertia relative to dense, non-porous rocks, as discussed above. In contrast to the abundant unresolved porosity, the volumetrically minor resolved cracks appear to have a disproportionately strong effect on thermal conductivity by constricting heat flow pathways, lowering thermal inertia further, as evidenced by our modeling, to the 150–400 J m^{-2} K^{-1} s$^{-½}$ range observed in Bennu's darkest boulders. This illustrates how the relationship between pore volume and thermal transport is nonlinear and strongly dependent on pore geometry, making it challenging to calculate total porosity and, consequently, strength from thermal inertia alone without constraints on internal structure (c.f. Grott et al., 2019; Rozitis et al., 2020).

Modeling studies (Hamm et al., 2025; Elder, 2024) have shown that even a single, well-placed crack below the surface of a Ryugu or Bennu boulder is sufficient to reduce the effective thermal inertia values derived via LIT for the Ryugu and Bennu samples to those measured by spacecraft on both asteroids. These models required cracks located ~5–9 mm below the surface, depending on rotation period, which is deeper than the domain of most of our numerical crack analyses and larger than many studied samples. However, an equivalent reduction can be achieved by a more tightly spaced series of cracks with natural imperfections that works to reduce their effective thermal resistivity. Bennu and Ryugu have different rotation periods and thus different diurnal thermal skin depths (~2 and 3 cm, respectively), yet both display similarly low effective thermal inertias. This similarity despite the different rotation periods suggests that the key control is not the presence of a single, maximally thermally resistive crack at the proper depth, but rather the characteristic properties of the boulder-forming materials that give rise to dense networks of imperfect, sub–skin-depth cracks. With crack spacings well below the length of the diurnal thermal waves on both bodies, the networks act to suppress conductivity and yield comparable thermal inertias.

Although the origin of the crack networks in the samples is not yet known, they are best interpreted as indigenous features rather than products of sample collection or return. For Bennu, the agreement between the PSFDs of the sampled particles and the sampling site suggests that extensive modification did not occur via this route. The controlled splitting tests demonstrated that even when particles do break apart along new fracture planes, they do not develop pervasive new internal cracks. The situation is less certain for Ryugu samples because the Hayabusa2 sampling mechanism (Sawada et al., 2017) was more energetic than OSIRIS-REx's (Bierhaus et al., 2018), potentially increasing the likelihood that particles were broken apart or selectively destroyed during collection. Nonetheless, the abundant crack networks observed in Ryugu samples closely resemble those in hummocky Bennu particles, and together with extensive remote-sensing evidence for in situ cracking on both asteroids, they are explained most straightforwardly as native features.

The observed cracks are consistent with formation on Bennu by thermal fatigue (Molaro et al., 2020; Delbo et al., 2022; Lucchetti et al., 2024) or micrometeoroid impacts (Ballouz et al., 2020; Keller & Thompson et al., 2025), or earlier geologic processes within or on Bennu's parent body, such as impacts or fluid reaction–driven volume changes. For example, volume-increasing reactions (e.g., hydration) may have produced polygonal fracture patterns like those observed in the angular stones, whereas volume-decreasing reactions (e.g., desiccation) may have produced fractal or dendritic patterns like in the hummocky stones (Okamoto and Shimizu, 2015). Petrologic analysis of hummocky particles identified cracks along clast boundaries that have been filled with magnetite and phosphate grains, which precipitated from fluids (Connolly and Lauretta et al., 2025), indicating the persistence of some cracks from the parent body epoch. These cracks may have even affected the parent body's thermal evolution (Nakamura et al., 2023; Soini et al., 2024).

The contrasting physical properties of the angular and hummocky Bennu lithologies probably reflect their divergent histories on the parent body. Angular particles appear to have undergone multiple episodes of aqueous alteration (Connolly and Lauretta et al., 2025), which may have acted to more effectively cement the phyllosilicate-rich matrix and infill some accretionary pores with coarse phyllosilicate pods or dolomite and magnesite (Connolly and Lauretta et al., 2025). In contrast, the hummocky particles, commonly breccias (Connolly and Lauretta et al., 2025), record at least one disruption event followed by lithification that may have only been partial, leaving poor connectivity between phyllosilicates that constitute the matrix and/or residual pore spaces from the pre-lithification accumulation of clasts. Although some cracks in hummocky particles are infilled with magnetite or phosphates from later fluid episodes (Connolly and Lauretta et al., 2025), perhaps they were insufficient to produce the more coherent, infilled fabric of the angular particles. These different aqueous alteration regimes may have been spatially segregated in the parent body. As such, the relative abundance of dark and bright boulders on Bennu and other carbonaceous rubble piles may depend on which regions of the parent body contributed to post-disruption reaccumulation (e.g., Michel & Ballouz et al. 2020).

The distinct cracking style of the hummocky particles appears tied to this alteration history. Although the presence of clasts strongly influences crack propagation, clasts alone are not sufficient to explain the difference: XCT data show evidence of possible clasts in some angular particles, yet these particles do not exhibit the pervasive cracking seen in hummocky material. This observation suggests that the regime of aqueous alteration was the primary control on crack development, rather than the presence or absence of putative clasts.

Bennu's global thermal inertia is controlled by the properties of its boulders, with only a minor contribution from comparatively rare exposures of fine (sub-centimeter) regolith (Rozitis et al., 2020; Cambioni et al., 2021). The distribution of the two dominant boulder types (dark and bright) controls thermal inertia variations across Bennu's surface (Rozitis et al., 2020). Our measurements reinforce this: the angular particles correspond to the bright boulders, whereas the hummocky, heavily cracked particles correspond to the dark boulders. Trends in thermal inertia vs. albedo among carbonaceous near-Earth asteroids (NEAs) may thus reflect variations in the relative proportion of bright and dark boulders on each body, as proposed by Rozitis et al. (2020).

Variations in bright and dark boulder proportions on carbonaceous asteroids could reflect the ratio present during rubble-pile accumulation or the effects of surface evolution. Angular particles, with higher density, greater nanoindentation hardness, and longer, sparser cracks, tend to cleave and fragment more readily, which may explain why bright boulders are absent from the largest boulder size classes on Bennu (DellaGiustina and Emery et al., 2019; Rozitis et al., 2020; Cambioni et al., 2021) and why the angular lithology, assuming it corresponds to the less abundant bright boulders, is disproportionately represented among large returned particles with preserved morphologies (Connolly and Lauretta et al., 2025). In contrast, the interlocking nature of the cracks in hummocky particles could allow the dark boulders to become densely fractured but resistant to comminution, enabling them to persist as the dominant population among Bennu's largest boulders. These differences imply that the surface of Bennu, and perhaps other carbonaceous rubble piles, may evolve over time as the ratio of bright to dark boulders shifts with progressive fragmentation and loss of brittle angular material.

Other asteroids may have very different histories. For example, NEA (3200) Phaethon, a top-shaped carbonaceous asteroid like Bennu, shows a striking hemispherical dichotomy in thermophysical properties, potentially corresponding to very fine regolith in the southern hemisphere (55 ± 60 J m^{-2} K^{-1} $s^{-½}$) and abundant boulders in the northern hemisphere (800 ± 400 J m^{-2} K^{-1} $s^{-½}$) (MacLennan et al., 2022). Phaethon may thus represent a counterpoint to Bennu in that it was initially composed of predominantly bright boulder material and subsequently dehydrated by intense perihelion heating (Takir et al., 2020), which over time produced a significant population of very fine regolith particles. However, we also caution that the low thermal inertia of the southern hemisphere could be instead interpreted as heavily fractured boulders rather than fine-grained regolith, based on lessons learned from OSIRIS-REx. The Destiny+ flyby mission (Ozaki et al., 2022) will reveal the true nature of this dichotomy.

Further generalizing our findings to the interpretation of remote sensing data from other types of NEAs — including stony asteroids such as (99942) Apophis, the target of the OSIRIS-APEX mission (DellaGiustina et al., 2023) — presents challenges. Stony asteroids are linked to ordinary chondrites, which have generally higher densities and thermal conductivities than carbonaceous chondrites (Opeil et al., 2012; 2020). Some ordinary chondrites exhibit crack networks (Soini et al., 2024), but without a porous and poorly lithified phyllosilicate matrix, crack-forming events may lead to brittle comminution, like Bennu's bright boulders, rather than persistent fracture networks. Stony asteroids visited by spacecraft have a broad range of thermal inertias, including 91 ± 24 J m^{-2} K^{-1} $s^{-½}$ for (152830) Dinkinesh (Jackson et al., 2025), 150 ± 50 J m^{-2} K^{-1} $s^{-½}$ for (1862) Eros (Delbo et al., 2015), 320 ± 70 J m^{-2} K^{-1} $s^{-½}$ for (65803) Didymos (Rozitis et al., 2024), and 750 ± 150 J m^{-2} K^{-1} $s^{-½}$ for (25143) Itokawa (Cambioni et al., 2019).

The thermal inertias of these stony asteroids appear to reflect differences in coverage by fine regolith (low thermal inertia) versus boulders (high thermal inertia for these types of asteroids), rather than trends in boulder type abundance as on carbonaceous asteroids like Bennu and Ryugu.

Itokawa's boulders have an estimated thermal inertia of 894 ± 122 J m^{-2} K^{-1} $s^{-½}$ (Cambioni et al., 2019), somewhat lower than ordinary chondrites (~1000–2500 J m^{-2} K^{-1} $s^{-½}$) (Opeil et al., 2012). This indicates that at least some degree of internal cracking may be able to persist in stony asteroid boulders. Curated meteorite specimens may be biased toward stronger, less-cracked material when selected for thermal conductivity measurement (Opeil et al., 2012, 2020), and additional filtering by physical properties likely occurred earlier during atmospheric entry (Warren, 2001; Shober et al., 2025a) and subsequent search and recovery (Shober et al., 2025b). Thus, for stony NEAs, internal cracks may reduce boulder thermal inertia to levels similar to carbonaceous bright boulders, whereas the combination of both porous matrices and dense crack networks, as seen in Bennu and Ryugu's dark boulders, produces the globally low values unique to carbonaceous NEAs.

References:

Ballouz, R.-L. et al. Bennu's near-Earth lifetime of 1.75 million years inferred from craters on its boulders. *Nature* **587**, 205–209 (2020).

Barnouin, O. S. et al. Shape of (101955) Bennu indicative of a rubble pile with internal stiffness. *Nat. Geosci.* **12**, 247–252 (2019). https://doi.org/10.1038/s41561-020-0643-9

Bierhaus, E. B. et al. The OSIRIS-REx Spacecraft and the Touch-and-Go Sample Acquisition Mechanism (TAGSAM). *Space Sci. Rev.* **214**, 107 (2018).

Bruck Syal, M., Owen, J. M. & Miller, P. L. Deflection by kinetic impact: Sensitivity to asteroid properties. *Icarus* **269**, 50–61 (2016).

Burke, K. N. et al. Particle size-frequency distributions of the OSIRIS-REx candidate sample sites on asteroid (101955) Bennu. *Remote Sens*. **13**, 1315 (2021).

Cambioni, S. et al. Fine-regolith production on asteroids controlled by rock porosity. *Nature* **598**, 49–52 (2021).

Cambioni, S. et al. Constraining the thermal properties of planetary surfaces using machine learning: Application to airless bodies. *Icarus* **325**, 16–30 (2019).

Cheng, A. F. et al. AIDA DART asteroid deflection test: Planetary defense and science objectives. *Planet. Space Sci.* **157**, 104–115 (2018).

Connolly Jr., H. C. & Lauretta, D. S., et al. An overview of the petrography and petrology of particles from aggregate sample from asteroid Bennu. *Meteorit. Planet. Sci.* **60**(5), 979–996 (2025). https://doi.org/10.1111/maps.14335.

Daly, R. T. et al. Successful kinetic impact into an asteroid for planetary defence. *Nature* **616**, 443–447 (2023). https://doi.org/10.1038/s41586-023-05810-5

Delbo, M. et al. Alignment of fractures on Bennu's boulders indicative of rapid asteroid surface evolution. *Nat. Geosci.* **15**, 453–457 (2022). https://doi.org/10.1038/s41561-022-00940-3

Delbo, M., Mueller, M., Emery, J. P., Rozitis, B. & Capria, M. T. Asteroid thermophysical modeling, in *Asteroids IV* (eds Michel, P. et al.) 107–128 (University of Arizona Press, 2015).

DellaGiustina, D. N. et al. OSIRIS-APEX: An OSIRIS-REx Extended Mission to Asteroid Apophis. *Planet. Sci. J.* **4**, 198 (2023).

DellaGiustina, D. N. et al. Variations in color and reflectance on the surface of asteroid (101955) Bennu. *Science* **370**, eabc3660 (2020).

DellaGiustina, D. N., Emery, J. P., et al. Properties of rubble-pile asteroid (101955) Bennu from OSIRIS-REx imaging and thermal analysis. *Nat. Astron.* **3**(4), 341–351 (2019).

Elder, C. M. Thermal Inertia on Bennu: Explanation of Remote Sensing Observations and Predictions for Samples. 55th Lunar and Planetary Science Conference, abstract #2590 (2025).

Emery, J. P. et al. Thermal infrared observations and thermophysical characterization of OSIRIS-REx target asteroid (101955) Bennu. *Icarus* **234**, 17–35 (2014).

Flynn, G. J., Consolmagno, G. J., Brown, P. & Macke, R. J. Physical properties of the stone meteorites: Implications for the properties of their parent bodies. *Chem. Erde* **78**, 269–298 (2018).

Friedrich, J. M. et al. Physical properties, internal structure, and the three-dimensional petrography of CI chondrites. *Meteorit. Planet. Sci.* **60**(3), 632–645 (2025). https://doi.org/10.1111/MAPS.14320

Grott, M. et al. Macroporosity and grain density of rubble pile asteroid (162173) Ryugu. *J. Geophys. Res. Planet.* **125**, e2020JE006519 (2020).

Grott, M. et al. Low thermal conductivity boulder with high porosity identified on C-type asteroid (162173) Ryugu. *Nat. Astron.* **3**, 971–976 (2019).

Hamm, M. et al. Low thermal inertia of (162173) Ryugu a result of horizontal cracks in boulders. *Icarus* 116484 (2025).

Hamm, M., Pelivan, I., Grott, M., de Wiljes, J. Thermophysical modelling and parameter estimation of small Solar system bodies via data assimilation. *MNRAS* **496**, 2776–2785 (2020).

Hildebrand, A. R. et al. The fall and recovery of the Tagish Lake meteorite. *Meteorit. Planet. Sci.* **41**(3), 407–431 (2006).

Ishimaru, K. & Lauretta, D. S. Analysis of layered boulders on asteroid (101955) Bennu and their implications for fluid flow on the parent body. *Meteorit. Planet. Sci.* **59**(1), 193–210 (2024).

Ishizaki, T. et al. Measurement of microscopic thermal diffusivity distribution for Ryugu sample by infrared lock-in periodic heating method. *Int. J. Thermophys.* **44**, 51 (2023). https://doi.org/10.1007/s10765-023-03158-6

Jackson, S. L., Emery, J. P., Rozitis, B., Christensen, P. R., Spencer, J. R., et al. Thermal-IR Observations of (152830) Dinkinesh during the Lucy Mission Flyby. *Planet. Sci. J.* **6**, 168 (2025).

Jawin, E. R. et al. Physical, thermal, and spectral properties of Bennu's global boulder population. 56th Lunar and Planetary Science Conference, abstract #1481 (2025).

Jawin, E. R. et al. Boulder diversity in the Nightingale region of asteroid (101955) Bennu and predictions for physical properties of the OSIRIS-REx sample. *J. Geophys. Res. Planets* **128**, e2023JE008019 (2023). https://doi.org/10.1029/2023JE008019

Kaplan, H. H. et al. Bright carbonate veins on asteroid (101955) Bennu: Implications for aqueous alteration history. *Science* **370**(6517) eabc3557 (2020).

Keller, L. P. & Thompson, M. S., et al. Space weathering effects recorded in Bennu samples. *Nat. Geosci.* 18, 825–831 (2025). https://doi.org/10.1038/s41561-025-01745-w

Lauretta, D. S. & Connolly, H. C. Jr., et al. Asteroid (101955) Bennu in the laboratory: Properties of the sample collected by OSIRIS-REx. *Meteorit. Planet. Sci.* **59**, 2453–2486 (2024).

Lauretta, D. S. et al. Spacecraft sample collection and subsurface excavation of asteroid (101955) Bennu. *Science* **377**, 285–291 (2022).

Lauretta, D. S. & DellaGiustina, D.N., et al. The unexpected surface of asteroid (101955) Bennu. *Nature* **568**, 55–60 (2019). https://doi.org/10.1038/s41586-019-1033-6

Lauretta, D. S. et al. The OSIRIS-REx target asteroid (101955) Bennu: Constraints on its physical, geological, and dynamical nature from astronomical observations. *Meteorit. Planet. Sci.* **50**(4), 834–849 (2015).

Lucchetti, A. et al. Fast boulder fracturing by thermal fatigue detected on stony asteroids. *Nat. Commun.* **15**, 6206 (2024). https://doi.org/10.1038/s41467-024-50145-y

MacLennan, E., Marshall, S., & Granvik, M. Evidence of surface heterogeneity on active asteroid (3200) Phaethon. *Icarus* **388**, 115226 (2022).

Mellon, M. T., Fergason, R. L. & Putzig, N. E. The thermal inertia of the surface of Mars, in *The Martian Surface: Composition, Mineralogy, and Physical Properties* (Cambridge University Press, 2008).

Michel, P. Physical properties of Near-Earth Objects that inform mitigation. *Acta Astronaut.* **90**, 6–13 (2013).

Michel, P., Ballouz, R.-L., Barnouin, O.S., et al. Collisional formation of top-shaped asteroids and implications for the origins of Ryugu and Bennu. *Nat. Commun.* **11**, 2655 (2020).

Miyazaki, A. et al. A newly revised estimation of bulk densities and examination of the shape of individual Ryugu grains. *Earth Planet. Space* **75**, 171 (2023).

Molaro, J. L. et al. In situ evidence of thermally induced rock breakdown widespread on Bennu's surface. *Nat. Commun.* **11**, 2913 (2020).

Nakamura, T., Engrand, C., Zolensky, M., Hamilton, V. E. & Fraeman, A. A. Sample return missions: Rosetta Stones returned from the first small bodies in the Solar System. *Space Sci. Rev.* **221**, 44 (2025).

Nakamura T., Matsumoto M., Amano, K., Enokido., Y., Zolensky, M. E., et al. Formation and evolution of carbonaceous asteroid Ryugu: Direct evidence from returned samples. *Science* **379**, eabn8671 (2023). doi:10.1126/science.abn8671

Nolan, M. C. et al. Shape model and surface properties of the OSIRIS-REx target asteroid (101955) Bennu from radar and lightcurve observations. *Icarus* **226**, 629–640 (2013).

Okada, T. et al. Highly porous nature of a primitive asteroid revealed by thermal imaging. *Nature* **579**, 518–522 (2020). https://doi.org/10.1038/s41586-020-2102-6

Okamoto, A. & Shimizu, H. Contrasting fracture patterns induced by volume-increasing and decreasing reactions: Implications for the progress of metamorphic reactions. *Earth Planet. Sci. Lett.* **417**, 9–18 (2015).

Opeil, C. P., Britt, D. T., Macke, R. J. & Consolmagno, G. J. The surprising thermal properties of CM carbonaceous chondrites. *Meteorit. Planet. Sci.* **55**, E1–E20 (2020). https://doi.org/10.1111/maps.13556

Opeil, C. P., Consolmagno, G. J., Safarik, D. J. & Britt, D. T. Stony meteorite thermal properties and their relationship with meteorite chemical and physical states. *Meteorit. Planet. Sci.* **47**, 319–329 (2012).

Ozaki, N., Yamamoto, T., Gonzalez-Franquesa, F., Gutierrrez-Ramon, R., Pushparaj, N. et al. Mission design of DESTINY+: Toward active asteroid (3200) Phaethon and multiple small bodies. *Acta Astronaut.* **196**, 42–56 (2022).

Rozitis, B. et al. Pre-impact Thermophysical Properties and the Yarkovsky Effect of NASA DART Target (65803) Didymos. *Planet. Sci. J.* **5**, 66 (2024).

Rozitis, B., Ryan, A. J., Emery, J. P., Nolan, M. C., Green, S. F., et al. High-Resolution Thermophysical Analysis of the OSIRIS-REx Sample Site and Three Other Regions of Interest on Bennu. *J. Geophys. Res. Planet.* **127**, e2021JE007153 (2022).

Rozitis, B. et al. Asteroid (101955) Bennu's weak boulders and thermally anomalous equator. *Sci. Adv.* **6**, eabc3699 (2020).

Ryan, A. J. et al. Rocks with extremely low thermal inertia at the OSIRIS-REx sample site on asteroid Bennu. *Planet. Sci. J.* **5**, 92 (2024). https://doi.org/10.3847/PSJ/ad2dff

Sawada, H., et al. Hayabusa2 Sampler: Collection of Asteroidal Surface Material. *Space Sci. Rev.* **208**, 81–106 (2017).

Scheeres, D. J. et al. The dynamic geophysical environment of (101955) Bennu based on OSIRIS-REx measurements. *Nat. Astron.* **3**, 352–361 (2019). https://doi.org/10.1038/s41550-019-0721-3

Scheeres, D. J. et al. Heterogeneous mass distribution of the rubble-pile asteroid (101955) Bennu. *Sci. Adv.* **6**, eabc3350 (2020). https://doi.org/10.1126/sciadv.abc3350

Soini, A.-J., Kukkonen, I. T., Suhonen, H., Lukić, B. & Luttinen, A. V. 3D porosity, flow, and transport characteristics of two L chondrites reveal wet accretion-related cosmic web-like porosity. *Planet. Space Sci.* **247**, 105915 (2024).

Shimaki, Y. et al. Thermophysical properties of the surface of asteroid 162173 Ryugu: Infrared observations and thermal inertia mapping. *Icarus* **348**, 113835 (2020).

Shober, P. M., Devillepoix, H. A. R., Vaubaillon, J., Anghel, S., Deam, S. E., et al. Perihelion history and atmospheric survival as primary drivers of the Earth's meteorite record. *Nat. Astron.* **9**, 799–812 (2025a).

Shober, P. M., Devillepoix, H. A. R., Vaubaillon, J., Samson, E. K., Deam, S. E., et al. What falls versus what we recover: Quantifying search and recovery bias for orbital meteorites. *Meteorit. Planet. Sci.* (2025b). https://doi.org/10.1111/maps.70041

Takir, D., Kareta, T., Emery, J. P., Hanuš, J., Reddy, V., Howell, E. S., Rivkin, A. S., & Arai, T. Near-infrared observations of active asteroid (3200) Phaethon reveal no evidence for hydration. *Nat. Commun.* **11**, 2050 (2020).

Walsh, K. J. et al. Numerical simulations suggest asteroids (101955) Bennu and (162173) Ryugu are likely second or later generation rubble piles. *Nat. Commun.* **15**, 5653 (2024).

Walsh, K. J., Delbo, M., Bottke, W. F., Vokrouhlický, D. & Lauretta, D. S. Introducing the Eulalia and new Polana asteroid families: Re-assessing primitive asteroid families in the inner Main Belt. *Icarus* **225**, 283–297 (2013). https://doi.org/10.1016/j.icarus.2013.03.005

Warren, P. H. Porosities of lunar meteorites: Strength, porosity, and petrologic screening during the meteorite delivery process. *J. Geophys. Res.* **106**, E5, 10101–10111 (2001).

Yokoyama, T., Nagashima, K., et al. Samples returned from the asteroid Ryugu are similar to Ivuna-type carbonaceous meteorites. *Science* **379**, eabn7850 (2023). https://doi.org/10.1126/science.abn7850

Zega, T. J., McCoy, T. J., et al. The micro- to nanoscale mineralogy of Bennu samples resulting from hydrothermal alteration. *Nat. Geosci.* 18, 832–839 (2025). https://doi.org/10.1038/s41561-025-01741-0

Acknowledgements

This material is based upon work supported by NASA Award NNH09ZDA007O and under Contract NNM10AA11C issued through the New Frontiers Program. We are grateful to the entire OSIRIS-REx Team for enabling the return and analysis of samples from asteroid Bennu. We thank the Astromaterials Acquisition and Curation Office, part of the Astromaterials Research and Exploration Science (ARES) Division at Johnson Space Center, for their efforts in recovery, preliminary examination, and long-term curation of the Bennu samples. We also greatly appreciate support from the OSIRIS-REx Sample Analysis Micro-Information System (SAMIS) Team. M.P. and F.T. were supported for this research by the Italian Space Agency (ASI) under the ASI-INAF agreement number 2022-1-HH.0. C.M.E. was supported by the OSIRIS-REx Participating Scientist Program (80NM0018F0612). Some of this work was carried out at the Jet Propulsion Laboratory, California Institute of Technology, under a contract with the National Aeronautics and Space Administration (80NM0018D0004). A.J.K. and H.C.B. acknowledge funding from UK Research and Innovation (UKRI) grant numbers MR/T020261/1 and MR/Y034333/1. The authors thank Dr. Masayuki Uesugi, Prof. Akira Tsuchiyama, and Prof. Tomoki Nakamura for sharing the XCT data of Ryugu sample C0002.

Author Contributions

A.J.R., R.-L.B., R.J.M., T.I., A.A., J.B., S.A.E., C.G.H., K.J.J., M.P., H.C.C. Jr., and D.S.L. conceptualized the study. A.J.R., R.-L.B., R.J.M., T.I., A.A., J.B., S.A.E., C.G.H., K.J.J., A.J.K., C.P.O., M.P., F.T., J.J.B., H.C.B., E.L.B., C.C., F.C., J.P.D., R.F., D.P.G., C.G., P.H., R.D.H., L.T.J.H., R.R., A.R.H., D.H., K.I., M.K.K., N.G.L., T.J.M., M.M., H.N., E.W.O., J.P., K.R., N.S., P.F.S., S.T. prepared samples for analysis, collected data, and analyzed data. A.J.R., R.-L.B., R.J.M., T.I., A.A., J.B., S.A.E., C.G.H., K.J., A.J.K., C.P.O., M.P., F.T., E.B.B., S.C., M.D., D.N.D., C.M.E., J.P.E., J.F., V.E.H., L.T.J.H., A.R.H., K.I., E.R.J., M.K.K., T.J.M., J.L.M., K.R., P.S., M.A.S., T.J.Z., C.W.V.W., H.C.C. Jr., and D.S.L. conducted data synthesis and interpretation of results. A.J.R., A.A., T.I., M.P., F.T., and J.B. drafted figures. A.J.R., R.-L.B., R.J.M., T.I., A.A., J.B., S.A.E., C.G.H., K.J., A.J.K., M.P., F.T., J.P.P., D.P.G., R.D.H., M.K.K., and N.G.L. drafted initial sections of the manuscript. A.J.R. compiled the manuscript. All authors reviewed the manuscript.

Methods

Samples

The samples studied (Supplementary Table 1) were retrieved from within the OSIRIS-REx Touch-and-Go Sample Acquisition Mechanism (TAGSAM) (Bierhaus et al., 2018) and are therefore denoted by IDs of the structure OREX-8#####-#. OREX-800107-103, OREX-800107-104, and OREX-803009-102 are subsets of a homogenized powder that was generated from the crushing and homogenization of 6.425 g of aggregate sample OREX-800107-0 (Supplementary Information). OREX-800117-108 is a subset of homogenized powder of another aggregate sample (OREX-800117-0, 1.288 g) (Supplementary Information). OREX-800055-7, OREX-800055-8, and OREX-800055-9 were generated from the controlled splitting under pristine conditions of OREX-800055-0. OREX-800088-5 was generated from the controlled splitting of OREX-800088-0. The methods to produce both splits are described later in the Methods. All other samples used in this study are individual particles.

Lock-in thermography (LIT)

LIT is a periodic method for measuring thermal diffusivity. The same technique with similar details in methodology has been used for the analysis of Ryugu samples (Ishizaki et al., 2023). A spot on the sample is periodically heated using a laser with a prescribed periodic pulse. The temperature response is measured by a thermal infrared camera, where the image acquisition rate is synchronized (“locked-in”) with the periodic heating frequency. The thermal diffusivity is analyzed from the gradient of the phase lag in the observed temperature according to this equation: $D = \pi f/(d\theta/dr)^2$. Here, D is thermal diffusivity, f is heating frequency, θ is phase lag, and r is distance from heating point. The system consists of thermal imagers (InfraTec ImageIR® 8350hp and Nippon Avionics Co., LTD. ThermoHAWK H9000) equipped with InSb cooled detector and 3× microscopic lens which provides a spatial resolution of 5 μm, optics, and a diode laser (633 nm, ~5 μm of focus diameter). The laser beam was modulated along the synchronized periodic signal from LIT. The output power of the laser was less than 6.7 mW. The heating frequency was selected from 0.5−40 Hz based on sample size and geometry in order to prevent thermal wave interference with the boundary of the sample or other topographic features outside of the area of interest. The samples were kept under vacuum of a pressure less than 10^{-2} Pa to eliminate heat transfer within the samples’ pore space. All measurements were conducted slightly above room temperature (~30–45°C).

Four samples were measured by LIT, including one hummocky particle (OREX-800118-0, ~50 mg) and three angular particles (OREX-800055-7, OREX-800055-8, and OREX-803009-102, ~2–3 mg each). Measurement sites on the samples’ surfaces are chosen to be qualitatively flat and sufficiently far from the sample edges or known large cracks to prevent thermal wave reflections. Nine measurement sites were analyzed on OREX-800118-0, and four measurement sites were analyzed on each of the three smaller, angular particles. At each measurement site, thermally diffusivity was determined in all directions radiating from the laser pulse at a 2° azimuthal resolution.

Thermal inertia values were calculated from thermal diffusivity as $TI = \sqrt{D\rho^2 c_p(T)^2}$, where D is the measured thermal diffusivity (Extended Data Table 1), ρ is sample density, and $c_p(T)$ is specific heat at temperature T as reported in Extended Data Table 1. The density of OREX-800118-0 and OREX-803009-102 was determined directly from XCT-based volumes and microbalance mass measurements, reported in Extended Data Table 2. The density of OREX-800055-7 and OREX-800055-8 was not measured directly but was assumed to be identical to the parent stone (OREX-800055-0) from which these split particles were derived. Mass and volume measurements of other larger fragments from OREX-8000055-0 indicate that this assumption is valid to within 5%. The specific heat results for a representative powdered aggregate sample (Extended Data Fig. 1; methods described in the next section) are assumed for all samples. Although specific heat is dependent on mineralogy and thus may vary between samples, these variations in specific heat are not expected to exceed 5%. The combined uncertainty of these assumed density and specific heat values in calculated thermal inertia thus would not exceed approximately 10%.

The mean sampling depth of the LIT thermal wave was estimated from the assigned measurement frequency and the measured thermal diffusivity result using the equation for the double e-folding depth of the thermal wave (where the thermal wave would be attenuated to only ~14% of its original magnitude). The equation is, $d = 2\sqrt{D/f\pi}$ where f is the laser pulse frequency (Hertz) as reported in Extended Data Table 1.

The presence of cracks near the LIT heating point can affect measurements in three different ways. The first case is when the distance from the heating point to the crack is sufficiently large, i.e., beyond the sampling depth described above. Because temperature waves attenuate as they propagate and thus many cracks are simply too far away to be sensed. Therefore, the measured result obtained represents the thermal diffusivity of the pure matrix.

The second case is when the temperature wave passes through a crack that has a relatively low thermal resistivity, allowing detection of phase lag before and after the crack. In this case, by using the phase lag before and after the crack, an effective thermal diffusivity that takes into account both the thermal diffusivity of the matrix and the thermal resistance due to the crack can be obtained as the measurement result. The thermal resistivity of a crack is primarily controlled by the size and number of contacts between the two opposing planes that constitute the crack (including contacts or "thermal bridges" created by infilling mineral precipitates) and the distance between the planes (i.e., crack thickness). If the distance is smaller than the wavelengths of radiative heat transfer, near-field radiative transfer effects (evanescent waves) are introduced, which can exceed those of classical Stefan-Boltzmann law by orders of magnitude. Near-field effects are proportional to the inverse square of the gap size and may become significant in cracks narrower than a few microns (Persson and Biele, 2022).

The third case is when the heating point is located near a crack and temperature wave is completely blocked by the crack, and the measured phase lag is interrupted at the crack. In this case, since the measured phase lag is affected by the reflected waves, the fundamental experimental assumptions are violated, and the thermal diffusivity cannot be accurately calculated without introducing an erroneous over- or underestimation.

Specific heat measurements

DSC (differential scanning calorimetry) measurements from 225 to 405 K were performed at Nagoya University with OREX-803224-0 (13.804 mg), a subset of a homogenized powder from OREX-800107-0. The sample powder was containerized in aluminum pans and not fully sealed to allow physiosorbed water to evaporate and diffuse out into the dry purging gas. The sample was heated and kept at 130°C (403.15 K) while purged in high-purity N_2 within the DSC instrument for 120 min to evaporate any adsorbed water before starting the measurements. It was discovered that water adsorption on Bennu samples is a critical issue. The sample mass quickly increases by about 4% due to water absorption with a time constant of ~30 minutes in laboratory air of relative humidity 46%.

The DSC instrument is a power-compensated Perkin Elmer-DSC 8000 measurement system with Intercooler II as cooling system and high-purity N_2 as purging gas. The measurement procedure is the 3-curve technique (empty, reference, sample) with the step-scan method (Cezairliyan and Ho, 1988) to eliminate most systematic instrument drifts; this method can be accurate to better than ±1%. Reference samples were sapphire (corundum, α-Al_2O_3) disks from Perkin Elmer with mass fraction purity of 0.9998; the reference specific heat was taken from Ditmars, Ishihara et al. (1982).

Low-temperature calorimetry (LTC) (3–260 K) via the hybrid adiabatic relaxation technique was performed with the Quantum Designs Physical Properties Measurement System (PPMS) at Boston College (Opeil et al., 2020). Sample OREX-800107-104 (31.9 mg), another subset of a homogenized powder from OREX-800107-0, was pressed into a cylindrical pellet 3 mm in diameter with a calculated volumetric bulk density of 2.56 ± 0.07 g cm^{-3}. The pellet was heated to 130°C for 48 hours in flowing high-purity argon to remove any absorbed water from the atmosphere. Following desiccation, the sample was exposed to lab air for approximately 8 minutes during which time it was weighed and then installed into the PPMS liquid helium cryostat for immediate measurement following the methods described in Opeil et al. (2020). A thin layer of Apiezon Type-N vacuum grease was used to improve the thermal contact between the sample puck and the sample pan. Following the measurement and subsequent ~6 hours of lab air exposure, a mass change of only ~0.7% was recorded, indicating that the pressed pellet was slower to absorb atmospheric water than the powdered DSC samples. This is likely due to the reduction in internal porosity from the pellet pressing process, leading to a lower diffusion rate in the sample. The results of the LTC and DSC measurements are shown in Extended Data Figure 1. The two datasets agree within their uncertainties (approximately ±1%) within the temperature range where the measurements overlap (225–260 K).

Structured light scanning (SLS), laser scanning, and X-Ray computed tomography (XCT)

SLS and XCT measurements of large particles (tens to thousands of milligrams each, 20.7 g total) were conducted under curation-pristine conditions at NASA JSC (Lauretta and Connolly et al., 2024; Righter et al., 2023) with a Polyga Compact C506 SLS and a Nikon XTH 320 XCT instrument, respectively. All particles analyzed with these techniques are listed in Extended Data Table 2. XCT data were segmented using standard threshold-based procedures to extract 3D models of each particle for volume and ultimately density calculations. Large internal voids and visible cracks, including those that intersect the surface, were infilled during the segmentation using a series of dilation and infill steps followed by erosion steps to return the segmentation to its original size. The resulting XCT-segmented shape models are generally sharper than SLS models. Although the relative loss of sharpness in SLS models may influence bulk volume and density comparisons, the effect is likely minimal given that the rounding/smoothing can be both subtractive (e.g., removing sharp corners) and additive (e.g., infilling crevices). We find that SLS models are slightly inflated compared to the XCT models, leading to an average volume difference of 1%, indicating a possible difference in dimensional calibration between the two instruments. To bring the two datasets into agreement for the analysis of density trends in the sample population, we increase XCT volumes by 1% in Extended Data Table 2. We assign a 1% uncertainty to all sample volumes (SLS and XCT) in Extended Data Table 2 to account for additional dimensional calibration uncertainty, XCT segmentation inaccuracies, and the rounding of features in SLS data.

OREX-800118-0 underwent higher-resolution XCT measurements at the University of Texas High-Resolution X-Ray CT (UTCT) Facility with a Zeiss Xradia 620 Versa XCT instrument. The particle was positioned within a polyethylene pipette tip for scanning. The full particle was scanned using the flat panel detector at 80 kV and 10 W using an LE3 filter with 4501 views collected with an exposure time of 0.08 s (20 exposures per view). The scan was reconstructed into a 3D volume using the Xradia Reconstructor software with a beam hardening correction of 0.38 and at a voxel size of 3.12 µm.

OREX-803009-102 underwent XCT scanning at the University of Arizona with a Shimadzu inspeXio SMX-225CT FPD HR Plus Microfocus X-ray CT System. The particle was positioned in a 0.2 mL polypropylene microcentrifuge tube for scanning. The entire particle was scanned using the flat panel detector at 80 kV and 3.2 W with 684 radiographs collected at exposure times of 0.25 s as the sample rotated 360° four times. The radiographs were reconstructed into a three-dimensional (3-D) volume using Dragonfly software at a voxel size of 3.56 µm.

The classification of the Bennu samples (angular, hummocky, or mottled) in Extended Data Table 2 is based on the morphological descriptors and example images from Lauretta & Connolly et al. (2024) and Connolly & Lauretta et al. (2025), and thus is subjective.

In addition to Bennu samples, we also measured density values for three meteorites. The shapes and volumes of samples of Tarda (VO Cat#1602) and Aguas Zarcas (VO Cat#1599) were laser-scanned at the Vatican Observatory (VO) using a NextEngine model 202i laser scanner with ProScan and Ultrares software upgrades, scanning at approximately 45 points per square millimeter with multiple (up to 45) overlapping scan orientations. Alignment, artifact removal, and creation of a watertight shape model were performed within the NextEngine software. Specimen volume was calculated with Geomagic Verify software. The shape and volume of a sample of Oued Chebeika 002 was measured via SLS at the University of Arizona under ambient laboratory conditions but otherwise using the same instrument and techniques described here for SLS measurements at NASA JSC. The mass and density values for these meteorites, as well as others from pre-existing sources, are reported in Extended Data Table 2.

X-ray diffraction (XRD), grain density, and porosity

The mineralogy of homogenized powder specimens OREX-800107-103 (48.8 mg) and OREX-800117-108 (54.9 mg) was determined using position sensitive detector X-ray diffraction (XRD) at the Natural History Museum (NHM), London. The powdered samples were loaded into an aluminum sample well using a stainless steel spatula, and diffraction patterns were acquired using an Enraf-Nonius PDS120 X-ray diffractometer equipped with an INEL curved 120° PSD. Samples were rotated continuously throughout an analysis, with the detector remaining in a static geometry relative to the primary X-ray beam (Cu Kα1) and sample stage. X-ray diffraction patterns were collected from OREX-800107-103 and OREX-800117-108 for 16 hours, and from mineral standards prepared in the same way for 30 minutes. The instrument was calibrated using silicon and silver behenate standards, and the intensity of the primary beam was monitored at regular intervals using a polished Fe-metal block.

Mineral abundances were quantified using a profile-stripping method (Cressey and Schofield, 1996; Schofield et al., 2002; King et al., 2015). Briefly, the XRD pattern of a mineral standard was scaled to the same measurement time as the samples (e.g., ×32 for a 16-hour measurement), before being reduced by a factor until it matched its intensity in the pattern of the sample. Standard mineral patterns were then subtracted from the sample patterns to leave a residual that eventually reached approximately zero counts. Detection limits were better than 0.5 vol.% for crystalline phases and ~1% vol.% for phyllosilicate phases, with absolute uncertainties on the order of ~<1–5 vol%, depending on the crystallinity of the phase (King et al., 2015).

The average grain density of the two samples was calculated using the XRD mineral abundances, an estimate of the absolute mass of organic material and trace minerals, and standard mineral grain density values (Bland et al., 2004, Biele et al., 2022, Ahrens, 1995) (Extended Data Table 3). Organic material abundance was determined from measured carbon bulk abundance, carbon in carbonates, and carbon mass fraction in organic isolates (Foustoukos, et al., 2025). The resulting grain density values for both samples were 2.8 ± 0.1 g cm^{-3}, from which we calculated porosity estimates for the hummocky and angular samples using the respective class-average bulk density values and the total porosity of the asteroid.

A direct measurement of porosity was attempted via ideal gas pycnometry with many of the largest Stones of Interest (SOIs) described in Lauretta & Connolly et al. (2024). This instrument used high-purity nitrogen rather than helium due to noble gas mitigation requirements for maintaining sample pristinity. The grain density results were unrealistically high. Although the two gases produce comparable results in studies on meteorites, in the pristine glove box environment of the Bennu samples, the nitrogen likely adhered to the high internal surface area of the fine-grained phyllosilicate matrix, violating ideal-gas assumptions. This effect is normally mitigated by adsorbed atmospheric moisture in meteorites, but not in the pristine Bennu specimens. The results could not be interpreted without further investigation (Macke et al., 2024).

Segmentation and thermal modeling of cracked samples

We utilized machine learning to label and extract crack networks from XCT data. This approach was chosen for its ability to identify cracks at single voxel and sub-voxel scales that are recognizable by eye but difficult to extract with basic threshold segmentation methods. The Segmentation Wizard within the Dragonfly software platform was used to train a convolutional neural network (CNN) in the semantic segmentation of cracks and solid sample material. Training data consisting of three or four small subregions, typically a few millimeters in size, were initially hand-labeled. As the CNN predictions improved with more training data, the CNN itself was used to generate new training data that were hand-corrected in areas where predictions failed. This process was continued until nearly all visible cracks were correctly identified via visual inspection and a heuristic point of diminishing returns was reached. We utilized the built-in U-net convolutional network, which uses extensive data augmentation (e.g., flipping and warping of the training images) to produce a satisfactory result with a minimal training dataset, typically no more than four complete XCT slices or a similarly sized collection of smaller training frames. Training frames created later in the training and validation process were specifically chosen to include cracks that are narrower and more subtle. The resulting CNN was then applied to the entire dataset to segment cracks and voids from solid particle.

The cracks and voids were next dilated in 3D by 1 voxel before being exported as binary image stacks for thermal modeling. This dilation step works to fill some small gaps in crack planes that persisted as artifacts of the segmentation process. The thickness of the cracks is increased as a consequence of this step, but the effect of crack thickness on heat flow modeling is negligible.

The Porous Microstructure Analysis (PuMA) software package (Ferguson et al., 2018; 2021) was used to determine the reduction in thermal conductivity of the particles due to the presence of the cracks. We cropped the largest possible 3D rectangular region of XCT-derived cracks from the center of the particle, given that a rectangular volume is a requirement of the model. We utilized the conjugate gradient solver with a symmetric (and thus effectively insulating) boundary condition, which solves for the steady-state temperature distribution within the sample, where a constant, arbitrary heat flux is imposed on one face of the sample volume and a constant, arbitrary temperature is imposed on the opposing face. The thermal conductivity is then calculated using Fourier’s law of heat conduction based on the model-prescribed heat flux, the thickness of the sample, and the final temperature difference across the sample. This method is essentially a numerical reproduction of the experimental technique by Opeil et al. (2020). The thermal conductivity was calculated and reported along the longest axis of the rectangular region in order to capture the effects of the cracks at the largest length scale possible.

In the PuMA model, all voxels must be assigned fixed (temperature-independent) thermal conductivity values. In our case, we have two classes of voxels: those within a crack, and those within solid material. We used a solid material thermal conductivity of 0.5 W m^{-1} K^{-1} (a typical value for uncracked angular Bennu particles) and a crack conductivity of 5.0×10^{-5} W m^{-1} K^{-1} (approximately equivalent to a crack that is 15 μm wide radiating at a Bennu Nightingale sample site diurnal mean temperature of 260 K).

This methodology was applied to four hummocky particles and three angular particles (Extended Data Table 4), selected for the representative appearance of their crack networks in XCT data, to produce cropped rectangular regions (lengths 4.9–6.8 mm) for the thermal analysis with the PuMA model. The results are presented as a reduction in effective conductivity compared to the value assigned to the uncracked medium (Extended Data Table 4), such that the cracked sample thermal conductivity can be calculated by multiplying the thermal conductivity of the uncracked particle by the reported conductivity reduction factor. The conductivity reduction factors for the hummocky samples are 0.59–0.79, whereas the angular particles have reduction factors of 0.9–0.96. We found that varying the solid material and crack thermal conductivity values within a reasonable range (0.25–1.0 W m^{-1} K^{-1} and (1.0×10^{-5})–(5.0×10^{-4}) W m^{-1} K^{-1}, respectively) did not affect the overall resulting thermal conductivity reduction by more than about 1–2%, indicating that the reduction factor result is dominated by the high contrast in the thermal conductivity rather than the precise absolute values. This further indicates that conduction around (and constricted by) the cracks was the dominant heat transfer mechanism, rather than radiation across the crack gaps.

Particle size frequency distribution (PSFD)

The longest dimension of all resolvable particles was manually measured in ArcGIS using photos of all 12 trays containing OSIRIS-REx samples (16 μm/pixel) extracted from the interior of TAGSAM. The result includes 72,776 particles ranging from 0.03 to 36.6 mm (Extended Data Figure 4). The cumulative distribution displays 72,523 particles with diameters between 0.5 and 5.0 mm, 38 particles ≥10.0 mm, 8 particles ≥ 15.0 mm, and only two particles ≥20.0 mm. The mode, median, and mean of the entire dataset are 0.1 mm, 0.4 mm, and 0.6 mm, respectively.

Next, we applied published methodology (Clauset et al., 2009) to log-log cumulative particle size distribution, which is used to validate the existence of the power-law fitting model. The power-law index of this model, called α, is computed from its scaling parameter "α_{Cl}" through the following equation$\alpha = 1 - \alpha_{Cl}$ (Pajola et al., 2021; Pajola et al., 2024). The scaling parameter α_{Cl} is calculated using the maximum likelihood estimator. Moreover, this methodology provides the threshold value above which the power-law exists, called the completeness limit or $x_{\min}$. This threshold value is calculated through the Kolmogorov-Smirnoff (KS) statistics. We also estimated the uncertainty for these parameters with a nonparametric bootstrap procedure. This generates multiple synthetic datasets from a power-law random generator and performs several KS tests to verify whether the generated and observed data come from the same distribution. This procedure returns the p-value, a parameter that is used to quantify the plausibility of the power-law fitting curve hypothesis. A p-value of ≥0.1 suggests that any difference between the empirical data and the model can be explained with statistical fluctuations around the power-law distribution. On the other hand, a p-value <0.1 means that the dataset does not come from a power-law distribution (Clauset et al., 2009). The resulting power-law index of the sample PSFD is –2.1 ± 0.3 for particles larger than 1.1 mm, with a p-value of 0.81.

Splitting of particles

Particles were split under pristine conditions in a nitrogen glove box at the JSC curation facility (Righter et al., 2023). For each split, the sample was placed in the base of a stainless steel cylindrical vessel (Eagle Stainless STB Series Bottle). Stainless steel wafer tweezers (TDI 4WF-SA) were used as a chisel, placed against the sample and lightly tapped with a small steel ball pein hammer. The breaking of OREX-800055-0 required two strikes. The first strike was gentle, and the curation processor performing the split could feel that the particle did not break. The second was firmer (but with a swing arc of only ~5–10 cm) and successfully fragmented the particle. The particle was not difficult to break from the perspective of the curation processor who broke it. OREX-8000088-0 split on the first strike of the hammer, but this does not necessarily mean that it was easier to break. The two splits were conducted months apart and thus are difficult to directly compare. Images of the original and split stones are shown in Extended Data Figure 5.

Particle split and puzzle piece reconstruction

3D models of the particle fragments produced from the controlled splitting of OREX-800055-0 and OREX-800088-0 were generated from XCT scans, using the same methods described earlier in the Methods to determine density from segmented particle volume. The 3D models of the split particle fragments were next manually reassembled using the FlexScan3D commercial software, which allows for the manipulation of 3D surface mesh objects and the snapping of overlapping surfaces. This process was aided by comparing and fitting the split particle models against the XCT-based 3D model of each original, unsplit stone (Extended Data Figure 5).

Crack networks from the original unsplit stones were similarly segmented in Dragonfly via thresholding and exported as 3D models for comparison to the assemblies of the split particles. This allowed for the visual inspection of the relative number of new versus pre-existing fractures that were exploited when the particles were split.

Several large, unsplit particles were found to geometrically fit together by manual manipulation of their 3D models (from XCT or SLS) in 3D space, including a set of three mottled particles (OREX-800014-0, OREX-800023-0, and OREX-800073-0) and two angular particles (OREX-800017-0 and OREX-800020-0). The assembly of two additional particles was determined using Advanced Imaging and Visualization of Astromaterials (AIVA) images (Lauretta & Connolly et al., 2024) based on their surface morphology and surface textures: OREX-800021-0 and an unnamed particle present in aggregate sample OREX-800010-0 (Extended Data Figure 3).

Nanoindentation

Nanoindentation measurements were performed with an Ultra Nanoindentation Tester (UNHT^3) manufactured by Anton Paar with Bennu samples OREX-800088-5, split from a hummocky stone, and OREX-800055-9, split from an angular stone. Polished potted butts were prepared at JSC, where they were pressed into partially cured epoxy to help minimize epoxy penetration into the sample. The samples received a final polishing using broad ion beam milling.

Instrumented nanoindentation consists of pushing a three-sided pyramid Berkovich tip into the surface of a material and recording the force vs. displacement response, allowing for the properties of the sample (on a scale down to ~5–10 nm) to be elucidated thanks to phase separability (Ulm et al., 2010). The elastic modulus (M) and hardness (H) of the indented material(s) are determined using the Oliver and Pharr model (Oliver and Pharr, 2004). M is exclusively controlled by the elastic relaxation of the material, whereas H is affected by inelastic energy dissipation effects such as local crushing, densification and shear slippage under the probe, viscoelastic (time-dependent) effects, cracking, and material flow. As such, the scatter on M is typically smaller than that for H.

Nanoscale indentation tests were performed in fine-grained matrix regions of both samples using a force-controlled testing protocol with a maximum force of 1 mN. Grid locations for the mechanics of the clay matrix were chosen based on the appearance of having no inclusions that would dominate the indentation response (typically less than a 100 nm in diameter, which is close to the pixel limit of the 1000× microscope attached to the UNHT). The load-hold-unload time was 15-5-15 s. 265 points were sampled across five distinct locations in OREX-800055-9 with an average indentation depth of approximately 300 nm, residual depth (after elastic recovery) of 160 nm, and width (measured edge-to-edge along one side of the triangular pit outline) of 2000 nm. 62 points were sampled in three locations on OREX-800088-5 with an average indentation depth of approximately 400 nm, residual depth of 250 nm, and width of 3200 nm.

Data Availability

The instrument data products underlying the findings of this work is available via AstroMat.org at the DOIs given in Supplementary Table 1. Crack and pore networks segmented from XCT data for use in our thermal analysis are available in Ryan, 2025. The aligned 3D models from XCT and SLS of the puzzle piece particles (Extended Data Figure 3) and the split particles (Extended Data Table 5) are available in the same archive.

Methods-Only References:

Ahrens, T. J. *Mineral Physics and Crystallography: A Handbook of Physical Constants* (American Geophysical Union, 1995).

Biele, J., Grott, M., Zolensky, M. E., Benisek, A. & Dachs, E. The specific heat of astro-materials: Review of Theoretical concepts, materials, and techniques. *Int. J. Thermophys.* **43**(9), 144, (2022). https://doi.org/10.1007/s10765-022-03046-5

Bland, P. A., Cressey, G. & Menzies, O. N. Modal mineralogy of carbonaceous chondrites by X-ray diffraction and Mössbauer spectroscopy. *Meteorit. Planet. Sci.* **39**, 3–16 (2004).

Cezairliyan, A. & Ho, C. Y., Eds. *Specific Heat of Solids. CINDAS Data Series on Material Properties* (New York: Hemisphere Publishing, 1988).

Clauset, A., Shalizi, C. R. & Newman, M. E. J. Power-law distributions in empirical data. *SIAM Rev.* **51**, 661–703 (2009).

Cressey, G. & Schofield, P. F. Rapid whole-pattern profile stripping method for the quantification of multiphase samples. *Powder Diffr.* **11**, 35–39 (1996).

Ditmars, D., Ishihara, S., Chang, S., Bernstein, G. & West, E. Enthalpy and heat-capacity standard reference material: Synthetic sapphire (a-Al2O3) from 10 to 2250 K. *J. Res. Natl. Bur. Stand.* **87**(2), 159–163 (1982).

Ferguson, J. C. et al. Update 3.0 to "PuMA: The Porous Microstructure Analysis" *SoftwareX* **15**, 100775 (2021).

Ferguson, J. C., Panerai, F. Borner, A. & Monsour, N. PuMA: The Porous Microstructure Analysis software. *SoftwareX* **7**, 81–87 (2018).

Foustoukos, D. I. et al. H, C, and N in samples with outer solar system heritage: Asteroid Bennu and the C2 ungrouped chondrites Tarda and Tagish Lake. 56th Lunar and Planetary Science Conference, abstract 1259 (2025).

King, A. J., Schofield, P. F., Howard, K. T. & Russell, S. S. Modal mineralogy of CI and CI-like chondrites by X-ray diffraction. *Geochim. Cosmochim. Acta* **165**, 148–160 (2015).

Macke, R. J. et al. Ideal-gas pycnometry on pristine Bennu specimens: Impossible densities and possible explanations. 86th Annual Meeting of the Meteoritical Society, abstract 6116 (2024).

Macke, R. J., Consolmagno, G. J. & Britt, D. T. Density, porosity, and magnetic susceptibility of carbonaceous chondrites. *Meteorit. Planet. Sci.* **46**, 1842–1862 (2011). https://doi.org/10.1111/j.1945-5100.2011.01298.x

Oliver, W. C. & Pharr, G. M. Measurement of hardness and elastic modulus by instrumented indentation: Advances in understanding and refinements to methodology. *J. Mater. Res.* **19**, 3–20 (2004). https://doi.org/10.1557/jmr.2004.19.1.3

Pajola, M. et al. Evidence for multi-fragmentation and mass shedding of boulders on rubble-pile binary asteroid system (65803) Didymos. *Nat. Commun.* **15**, 6205 (2024). https://doi.org/10.1038/s41467-024-50148-9

Pajola, M., Lucchetti, A., Senter, L. & Cremonese, G. Blocks size frequency distribution in the Enceladus tiger stripes area: Implications on their formative processes. *Universe* **7**(4), 82 (2021). https://doi.org/10.3390/universe7040082

Persson, B. N. J. & Biele, J. Heat transfer in granular media with weakly interacting Particles. *AIP Advances* **12**, 105307 (2022.

Righter, K. et al. Curation planning and facilities for asteroid Bennu samples returned by the OSIRIS-REx mission. *Meteorit. Planet. Sci.* **58**, 572–590 (2023).

Ryan, A. J. 3d models and crack networks in support of the manuscript entitled Low thermal inertia of carbonaceous asteroid Bennu driven by cracks observed in returned samples. figshare https://doi.org/10.6084/m9.figshare.30276397

Schofield, P. F., Knight, K. S., Covey-Crump, S. J., Cressey, G. & Stretton, I. C. (2002) Accurate quantification of the modal mineralogy of rocks when image analysis is difficult. *Mineral. Mag.* **66**(1), 173–184.

Ulm F. J. et al. Does microstructure matter for statistical nanoindentation techniques? *Cem. Concr. Compos.* **32**, 92–99 (2010).

Extended Data Figures and Tables

Extended Data Table 1. Lock-in thermography thermal diffusivity and calculated thermal inertia. Results are reported as the average and associated error of the solutions across all azimuthal angles for a given measurement position, and the maximum and minimum solutions, which each come from a specific azimuthal direction. Measurement positions correspond to those shown in Fig. 1. Mean sample temperature measurement and measurement frequency are provided for each measurement.

Measure-ment position	Sample temperature (°C)	Frequency (Hz)	Mean sampling depth (µm)	Mean diffusivity ± 1-σ (10^{-7} m^2/s)	Maximum diffusivity (10^{-7} m^2/s)	Minimum diffusivity (10^{-7} m^2/s)	Mean thermal inertia ± 1-σ (J m^{-2} K^{-1} $s^{-½}$)	Maximum thermal inertia (J m^{-2} K^{-1} $s^{-½}$)	Minimum thermal inertia (J m^{-2} K^{-1} $s^{-½}$)
OREX-800118-0 (hummocky)									
1	31.2	2	340	1.8±0.6	3.1	1.1	550±90	720	430
1	31.7	4	250	1.9±0.6	3.7	1.1	570±90	790	430
2	32.6	0.5	680	1.8±0.7	2.6	0.9	550±110	660	390
2	33.0	4	220	1.5±0.9	2.7	0.6	500±160	680	320
4	33.0	20	140	2.9±0.6	3.5	2.5	700±70	770	650
7	33.4	0.5	840	2.8±1.4	4.5	1.4	690±180	870	490
7	33.6	4	310	3.0±0.8	4.4	1.9	710±100	860	570
8	32.5	0.5	890	3.1±1.2	4	1.6	720±140	820	520
8	33.1	4	340	3.7±0.8	5.4	2.3	790±90	960	620
9	33.4	0.5	780	2.4±1.1	4.2	0.8	640±150	840	370
9	32.7	4	350	3.9±1.4	5.6	2.7	810±150	970	680
10	30.6	0.5	710	2.0±1.8	3.4	0.6	580±310	760	320
10	30.0	4	270	2.3±1.4	4.1	1.2	620±200	830	450
11	33.8	0.5	780	2.4±1.2	4.8	0.4	640±170	900	260
11	33.0	4	270	2.3±0.9	4.3	0.8	620±130	850	370
12	33.3	20	140	3.1±1.1	4.6	2	720±130	880	580
12	34.7	40	100	3.1±0.7	4.7	2.5	730±80	890	650
OREX-803009-102 (angular)									
1	44.1	20	151	3.6±0.4	4	2.7	820±50	870	710
3	44.3	40	111	3.9±1.3	4.3	3.3	860±150	900	790
4	42.6	20	156	3.8±0.3	4.2	3.3	840±30	890	790
6	41.3	20	151	3.6±0.3	4.2	2.8	820±30	880	720
OREX-800055-7 (angular)									
1	46.7	4	352	3.9±0.5	4.5	3	920±60	990	810
2	47.7	4	339	3.6±0.4	4.8	3.2	880±50	1020	830
3	47.1	4	357	4.0±0.5	4.4	3.5	930±40	980	870
4	51.0	20	158	3.9±0.3	4.2	3.6	920±60	960	890
OREX-800055-8 (angular)									
1	53.6	40	107	3.6±0.3	4.1	2.9	890±40	950	800
2	52.6	40	110	3.8±0.3	5.7	3.5	920±40	1120	880
3	55.9	40	110	3.8±0.5	4.7	3	920±60	1020	820
4	40.0	20	164	4.2±0.4	4.7	4	940±40	1000	920

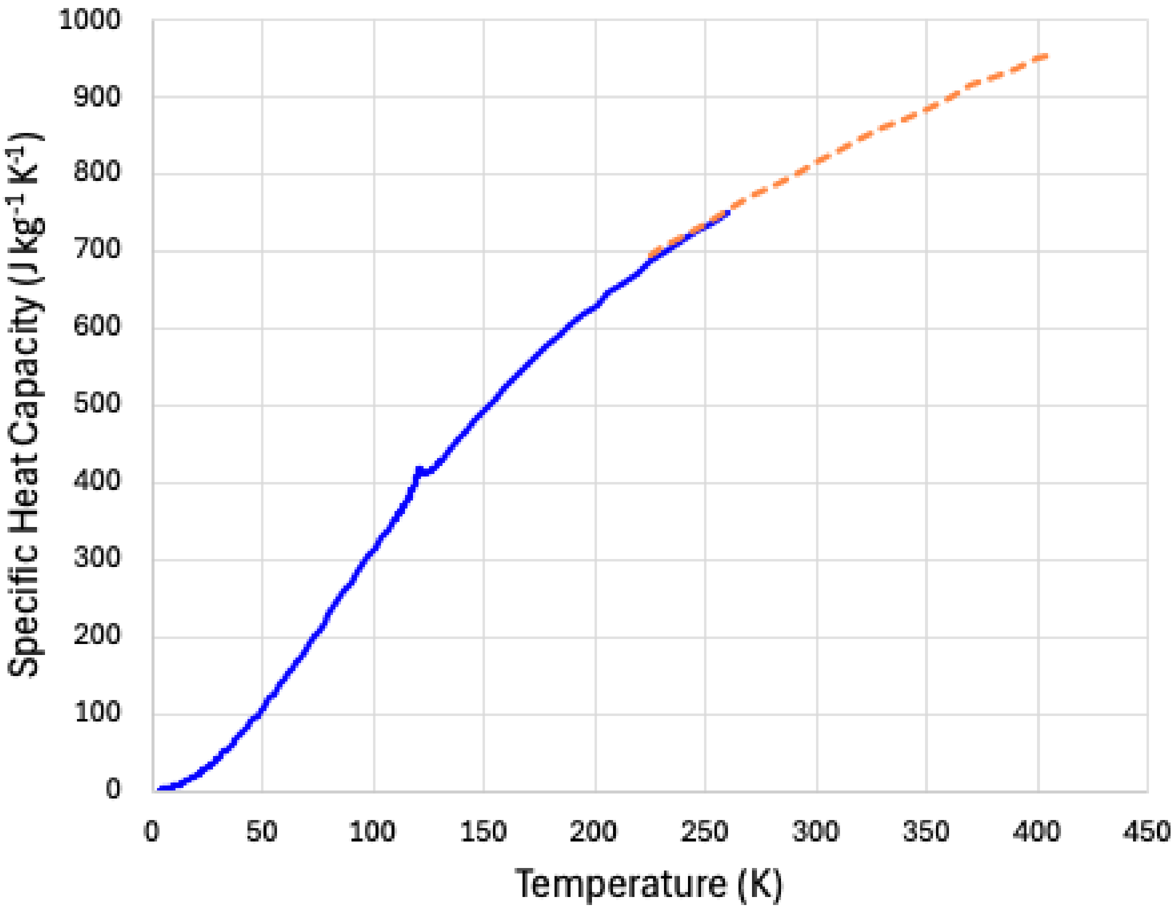

Extended Data Figure 1. Specific heat (c_p) of Bennu aggregate powder measured from 3 to 405 K. DSC, differential scanning calorimetry in solid blue; LTC, low-temperature relaxation calorimetry in dashed orange (Methods). Uncertainty decreases approximately linearly from ~8% to 1% between 3 K and 100 K and is ~1% above 100 K.

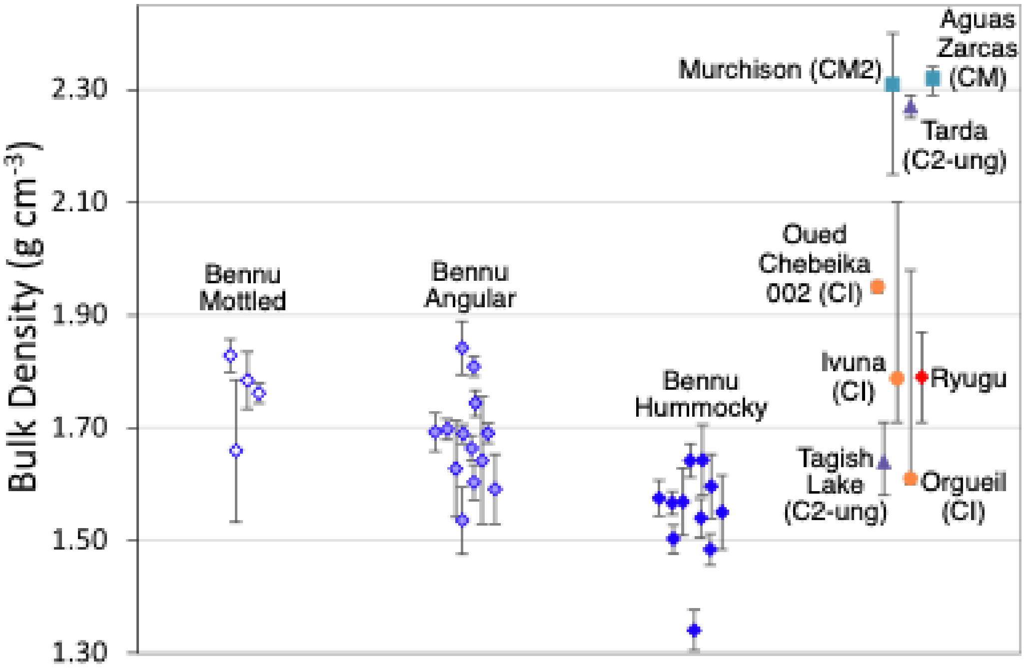

Extended Data Figure 2. Bulk density values for large (>50 mg) Bennu particles within the mottled, angular, and hummocky categories. Ryugu samples and possible meteorite analogs are shown for comparison. Data sources provided in Extended Data Table 2.

Extended Data Table 2. Densities of Bennu samples, Ryugu samples, and meteorites. The volume-weighted average density of meteorites with multiple specimens is denoted by the absence of a mass value. The classification of particles (mottled, angular, or hummocky) is based on external morphology and apparent brightness, as previously described (Lauretta & Connolly et al., 2024; Connolly & Lauretta et al., 2025). Samples denoted with an asterisk (*) were not included in Extended Data Figure 2 due to their very small size.

Bennu Samples						
Sample ID	**Mass (g)**	**Type**	**SLS density (g cm^{-3})**	**XCT density (g cm^{-3})**	**Density uncertainty**	**Reference**
OREX-800014-0	6.236	Mottled	1.761		0.02	Lauretta and Connolly et al. (2024)
OREX-800016-0	1.183	Angular	1.697		0.02	this work
OREX-800017-0	2.042	Angular	1.690		0.02	Lauretta and Connolly et al. (2024)
OREX-800018-0	2.896	Angular	1.809		0.02	this work
OREX-800019-0	2.251	Angular	1.689	1.696	0.02	SLS: Lauretta and Connolly et al. (2024); XCT: this work

OREX-800020-0	0.576	Angular	1.66		0.02	Lauretta and Connolly et al. (2024)
OREX-800021-0	0.592	Hummocky	1.57	1.59	0.02	SLS: Lauretta and Connolly et al. (2024); XCT: this work
OREX-800023-0	0.399	Mottled	1.83	1.87	0.03	SLS: Lauretta and Connolly et al. (2024); XCT: this work
OREX-800026-0	0.250	Hummocky	1.54		0.03	SLS: Lauretta and Connolly et al. (2024); XCT: this work
OREX-800027-0	0.134	Hummocky		1.55	0.07	this work
OREX-800047-0	0.150	Angular		1.59	0.06	this work
OREX-800049-0	0.153	Hummocky		1.57	0.06	this work
OREX-800054-0	0.076	Angular		1.64	0.11	this work
OREX-800055-0	0.591	Angular	1.74	1.74	0.02	SLS: Lauretta and Connolly et al. (2024); XCT: this work
*OREX-800055-7	0.003	Angular		*1.74*	*0.02*	*Density assumed from parent OREX-800055-0*
*OREX-800055-8	0.004	Angular		*1.74*	*0.02*	
OREX-800067-0	0.296	Angular	1.60	1.60	0.03	SLS: Lauretta and Connolly (2024); XCT: this work
OREX-800073-0	0.068	Mottled		1.66	0.13	this work
OREX-800087-0	0.372	Hummocky	1.50		0.03	Lauretta and Connolly et al. (2024)
OREX-800088-0	0.329	Hummocky	1.64	1.70	0.03	SLS: Lauretta and Connolly et al. (2024); XCT: this work
OREX-800089-0	0.313	Hummocky	1.48	1.50	0.03	SLS: Lauretta and Connolly et al. (2024); XCT: this work
OREX-800096-0	0.251	Mottled		1.78	0.05	this work
OREX-800097-0	0.168	Hummocky		1.60	0.06	this work
OREX-800098-0	0.150	Angular		1.54	0.06	this work
OREX-800099-0	0.152	Hummocky		1.64	0.06	this work
OREX-800118-0	0.04878	Hummocky		1.57	0.03	this work
OREX-800123-0	0.291	Angular		1.69	0.03	this work
OREX-800129-0	0.316	Angular		1.84	0.05	this work
OREX-800134-0	0.103	angular		1.63	0.09	this work
OREX-800141-0	0.279	Hummocky		1.34	0.04	this work

*OREX-803009-102	0.00187	Angular		1.6(3)	0.12	this work
Other materials						
Name	**Mass (g)**	**Type**	**Density (g cm^{-3})**	**Density uncertainty (g cm^{-3})**		**Reference**
Ryugu	--	Asteroid sample	1.79	0.08		Nakamura et al. (2023)
Ivuna	--	CI	1.787	+0.313, –0.077		Friedrich et al. (2025)
Orgueil	--	CI	1.61	+0.37, –0.01		Friedrich et al. (2025)
Murchison	--	CM2	2.31	+0.09,–0.16		Macke et al. (2011)
Tagish Lake	--	C2-ungrouped	1.64	+0.07, –0.06		Hildebrand et al. (2006)
Aguas Zarcas	8.28	CM2	2.32	0.02		this work
Tarda	4.33	C2-ungrouped	2.27	0.02		this work
Oued Chebeika 002	2.59	CI	1.95	0.01		this work

Extended Data Table 3. **Abundance of individual mineral phases in powdered aggregate samples OREX-800107-103 and OREX-800117-108.** The abundances were measured via XRD (relative weight percentage), with the addition of undetected minor low-Ca pyroxene and amorphous organics based on previous Bennu sample analyses (Lauretta & Connolly et al., 2024; Foustoukos et al., 2024). Grain density values assumed for the purpose of calculating the average grain density of each sample are from Biele et al. (2022), except dolomite is from Ahrens (1955). Forsterite is assumed for olivine based on the bulk mineralogy of Bennu samples (Lauretta & Connolly et al., 2024).

Phase	OREX-800107-103			OREX-800117-108			Assumed density (g cm^{-3})
	XRD relative wt%	Absolute wt%	vol%	XRD relative wt%	Absolute wt%	vol%	
Phyllosilicates (serpentines and smectites)	68.9	64.97	70.4	70.4	65.58	69.1	2.6±0.2
Magnetite, Fe_3O_4	11.9	11.22	6.1	9.1	8.48	4.5	5.2±0.02
Pyrrhotite, $Fe_{6.83}Ni_{0.17}S_8$	10.7	10.09	6.2	11	10.25	6.1	4.58±0.05
Pentlandite, $(Fe_{1-x}Ni_x)_9S_8$	3.9	3.68	2.0	2.6	2.42	1.3	5.08±0.1
Dolomite, $CaMg(CO_3)_2$	1.5	1.41	1.4	1.6	1.49	1.4	2.89±0.05
Calcite, $CaCO_3$	0.6	0.57	0.6	0.7	0.65	0.7	2.72±0.05
Olivine (predominantly forsterite, Mg_2SiO_4)	2.5	2.36	2.1	4.7	4.38	3.7	3.22±0.1
Low-Ca pyroxene	--	0.80	0.7	--	0.80	0.7%	3.3±0.1
Organic compounds	--	4.90	10.6	--	5.95	12.5%	1.3±0.3

Extended Data Table 4. Results from the thermal conductivity model for cracked samples. The length denotes the long axis (along which heat flow was simulated) of a cropped rectangular volume from the center of each sample's XCT dataset. These reduction factors account for both cracks and non-planar voids segmented from the XCT data.

Sample ID	Morphology	XCT Voxel size (µm)	Length (mm)	Conductivity reduction factor
OREX-800021-0	Hummocky	8.00	6.40	0.75
OREX-800088-0	Hummocky	8.50	6.21	0.59
OREX-800089-0	Hummocky	9.50	6.18	0.79
OREX-800097-0	Hummocky	6.50	4.88	0.60
OREX-800055-0	Angular	8.50	6.80	0.90
OREX-800123-0	Angular	6.25	5.00	0.90
OREX-800129-0	Angular	6.25	5.00	0.96

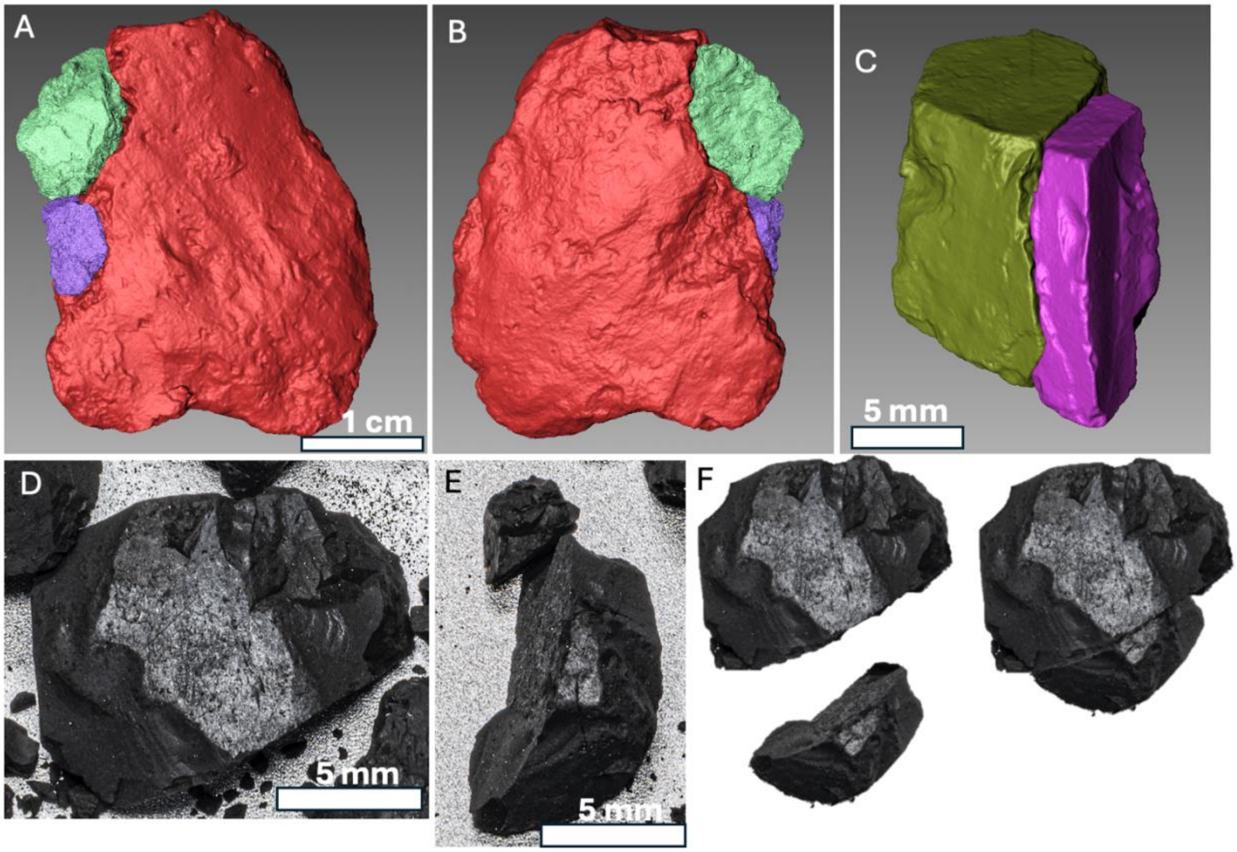

Extended Data Figure 3. Particles that can be geometrically reassembled like puzzle pieces. **(A, B)** 3D models (SLS, XCT) of three mottled particles, from largest to smallest: OREX-800014-0, OREX-800023-0, and OREX-800073-0. **(C)** 3D models (SLS, XCT) of two angular particles: OREX-800017-0 (larger) and OREX-800020-0 (smaller). **(D)** AIVA image of angular particle OREX-800016-0. **(E)** AIVA image of an unnamed particle within aggregate sample OREX-800010-0. **(F)** Photo-based assembly of OREX-800016-0 and the unnamed particle.

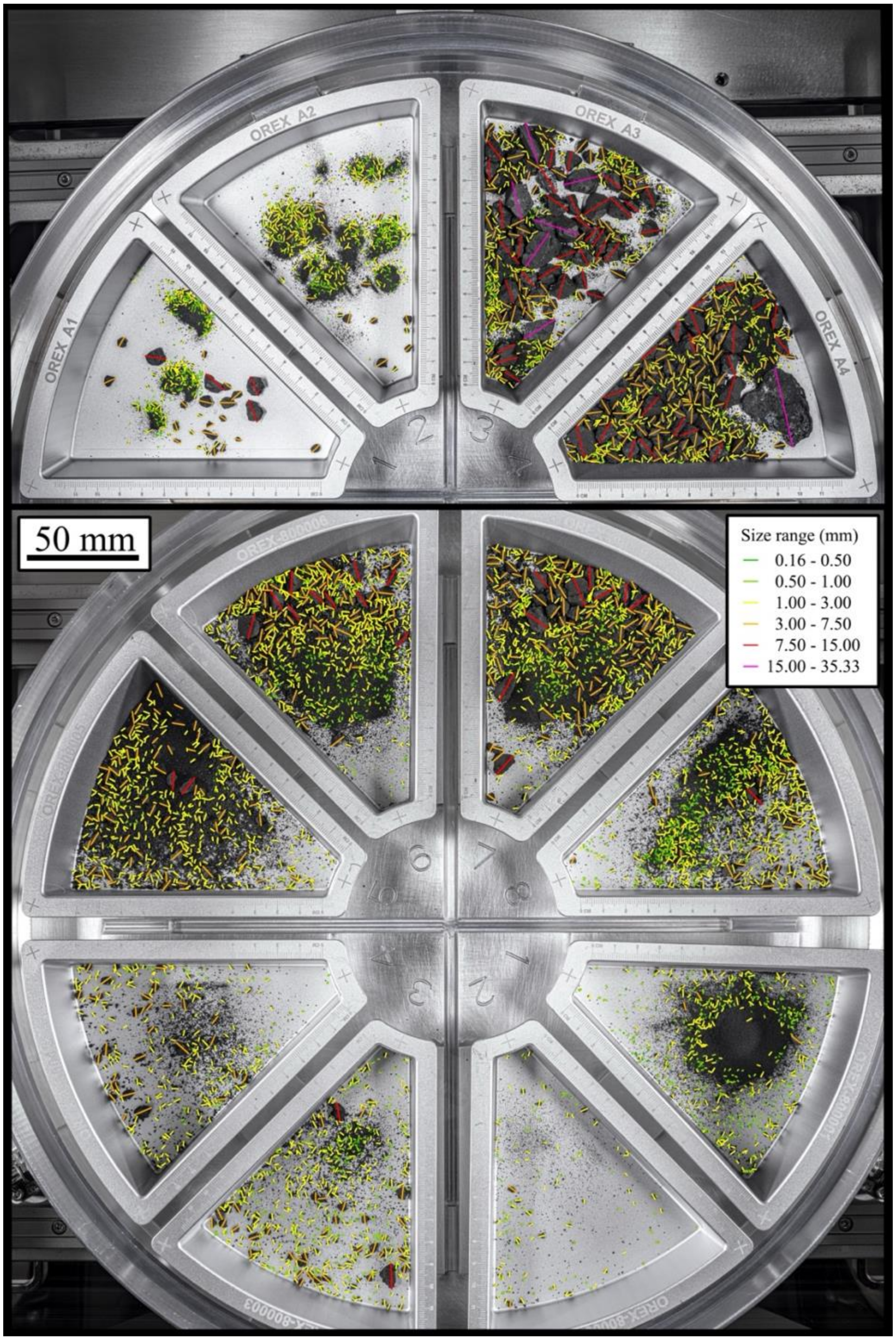

Extended Data Figure 4. **Particle long axes measured for the PSFD analysis, overlain on AIVA images of the complete sample collection from within TAGSAM.**

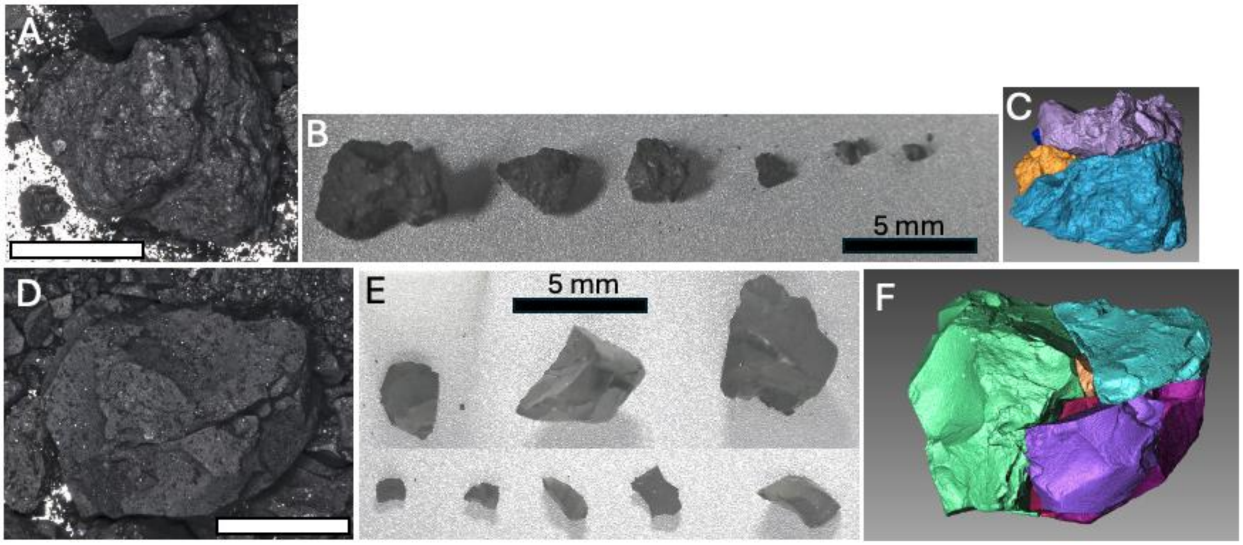

Extended Data Figure 5. Stones subjected to controlled splits. All scale bars are 5 mm. **(A)** AIVA image of hummocky sample OREX-800088-0. **(B)** Fragments produced from the split of OREX-800088-0. **(C)** Assembly of XCT models of large fragments of OREX-800088-0, excluding the largest fragment, which was set aside for thin sectioning to reduce the risk of breaking. **(D)** AIVA image of angular sample OREX-800055-0. **(E)** Fragments produced from the split of OREX-800055-0. **(F)** Assembly of XCT models of large fragments of OREX-800055-0.

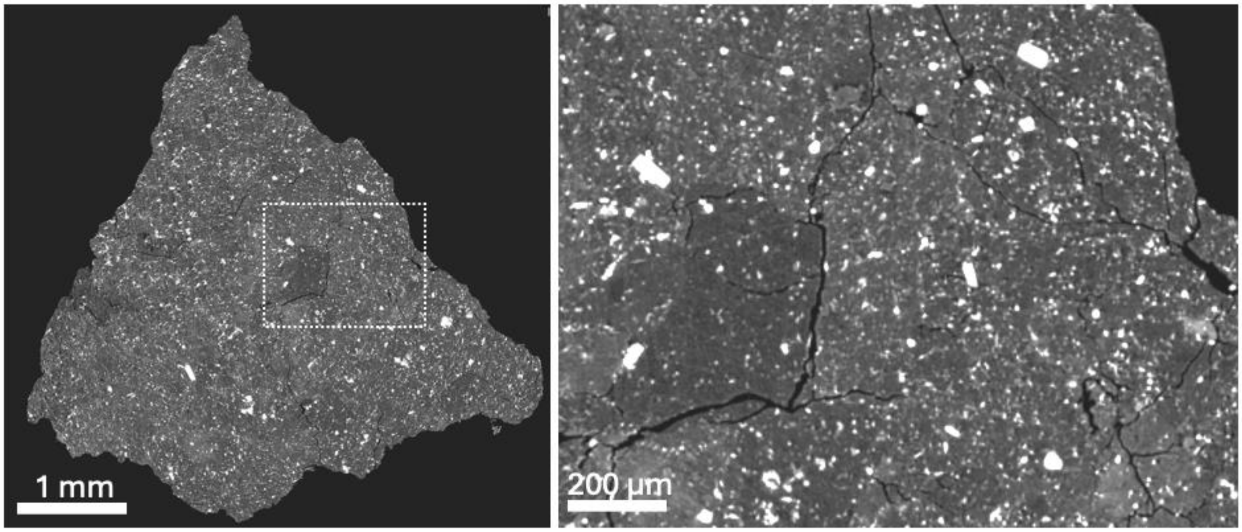

Extended Data Figure 6. XCT scan of Ryugu sample C0002. The dashed rectangle on the left corresponds to the zoomed view on the right showing details of internal crack networks.